Subsystem Development and Flight Testing of an Electroaerodynamic UAV

by

Cooper Curtis Hennick

B.S., Mechanical Engineering and Physics,
University of Wisconsin-Madison (2015)

Submitted to the Department of Aeronautics and Astronautics
in partial fulfillment of the requirements for the degree of

Master of Science in Aerospace Engineering

at the

MASSACHUSETTS INSTITUTE OF TECHNOLOGY

September 2017

Signature redacted

Author .....
Department of Aeronautics and Astronautics
August 24, 2017

Signature redacted

Certified by ....
Steven Barrett
Associate Professor of Aeronautics and Astronautics
Thesis Supervisor

Signature redacted

Accepted by ....
Hamsa Balakrishnan
Associate Professor of Aeronautics and Astronautics
Chair, Graduate Program Committee

Subsystem Development and Flight Testing of an Electroaerodynamic UAV

by

Cooper Curtis Hennick

Submitted to the Department of Aeronautics and Astronautics
on August 24, 2017, in partial fulfillment of the
requirements for the degree of
Master of Science in Aerospace Engineering

Abstract

Electroaerodynamic (EAD) propulsion is a form of in-atmosphere electric thrust generation with no direct emissions, no moving parts, and is nearly silent. Previous work has quantified the thrust-to-power and thrust density of EAD propulsion. An unmanned aerial vehicle (UAV) was designed with the optimization tool GPkit and with the flight mission goal of steady-level flight. This thesis describes the design and testing of several subsystems of the UAV, including the power system, the communication system, the aircraft tail, and the aircraft launching system. The power system is tested to deliver up to a maximum of 600 W at 40 kV. A system to collect flight data is also designed, based on a video camera and Kalman filter that measures the horizontal and vertical velocities of the aircraft throughout a flight. Seven powered, indoor flight tests on the order of 5 s are performed at a voltage level of 36.2 kV, 2.44 N of thrust, a thrust-to-power ratio of 7.2 N/kW and an average lift-to-drag ratio of 10.0. The average specific excess power (SEP) of the aircraft measured from the seven flight tests is -0.053 m/s.

Thesis Supervisor: Steven Barrett
Title: Associate Professor of Aeronautics and Astronautics

Contents

List of Figures

List of Tables

Chapter 1

Introduction

Electroaerodynamic (EAD) propulsion is a form of in-atmosphere electric propulsion where an ionic wind is created through the generation and acceleration of ions through an applied electric field. The ions collide with neutral air, transferring momentum to the ionic wind and producing a net force. Thrust generation is nearly silent, is accomplished with no moving parts, and as a form of electric propulsion, there are no direct emissions associated with fossil fuels.

The first empirical study of EAD for thrust generation was conducted by Christensen and Moller in 1967 [1], but since then, there have been few studies assessing the use of ionic winds for propulsion. Ionic winds have been studied for applications other than propulsion, including heat-transfer enhancement [2], ion drag pumps [3], and flow control over airfoils to prevent boundary layer separation [4].

But with the recent rise of drone technology, the continued and projected growth of the aviation sector [5], and findings that conventional aircraft propulsion negatively affects climate and public health through emissions [6] and noise [7], there has been increased motivation to develop electric means of propulsion, including EAD. Masuyama and Barrett [8] measured the thrust-to-power of a wire and tube (emitter and collector) EAD thruster and showed thrust-to-power ratios on the order of 5-10 N/kW, with achievable ratios up to 100 N/kW. The dependence of thrust T with voltage V was found to be

$$T = \frac{C'V(V - V_0)}{d}, \tag{1.1}$$

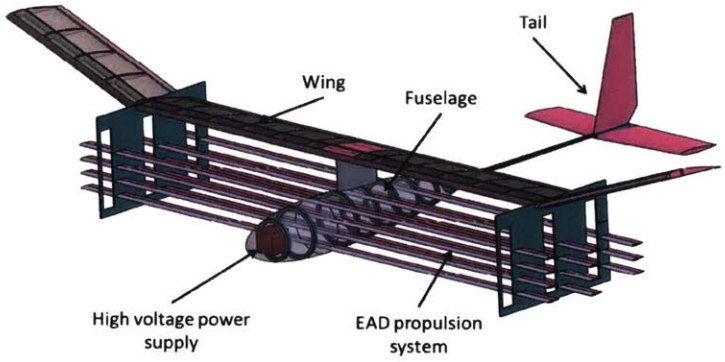

Figure 1-1: Design of the EAD-propelled UAV.

where C' is an empirical value dependent on the geometry, V_0 is the corona inception voltage (below which there is no thrust), and d is the gap spacing between the emitter and collector electrodes. The thrust T to power P relationship was found to be

$$\frac{T}{P} = \frac{d}{\mu V}, \tag{1.2}$$

where μ is the ion mobility. They also suggested that as multiple EAD thrusters are brought closer together, the interactions of electric fields could limit the thrust density of the EAD system. Gilmore and Barrett [9] measured the thrust density of similar wire-and-tube thrusters by arranging thrusters into both series and parallel arrays. Maximum thrust per unit frontal area and thrust per unit volume were found to be 3.3 $\mathrm{N/m^2}$ and 15 $\mathrm{N/m^3}$, respectively. The theoretical maximum thrust per unit frontal area was also derived. They compare to several aircraft and suggest that EAD propulsion is most likely applicable to the small unmanned aerial vehicle (UAV) size scale.

In his PhD thesis, Gilmore [10] designed a fixed-wing UAV powered by EAD propulsion with the aid of the optimization tool GPkit [11] with the objective of steady level flight for on the order of one minute. The design is shown in Figure 1-1. This thesis details the design and testing of several subsystems of that UAV, as well as a data collection system for flight tests, which are performed and analyzed.

Chapter 2

Subsystem design and manufacturing

This chapter describes the design and manufacturing of components within the aircraft's power system, communication system, aerodynamic structure, and the launching system. The power system comprises a battery stack, a high voltage power converter (HVPC), and the airframe thrusters. The communication system comprises components which provide the power switch signal and aircraft maneuver commands. A refinement to the main wing and the design of the tail will be discussed as part of the aircraft's aerodynamic structure. Finally, the launching system's mechanical and electrical design is presented.

2.1 Power system

The design and requirements of the battery stack, HVPC, and thrusters are discussed here. The HVPC is developed by He and Perrault [12] and most of the development work of the current thruster technology employed in the EAD aircraft owes to Masuyama and Barrett [8] and Gilmore and Barrett [9]. The overall system requirements are first given, and from there the individual components and their requirements are discussed in more detail, starting with the battery stack.

2.1.1 System requirements

The design goal of the power system is to deliver thrust to the aircraft for at least 60 s, which is sufficient for several straight-line indoor flight tests before the batteries require recharging. In order to allow for flexibility in the design point of the aircraft, the full system design from the GPkit model places a maximum power delivery requirement of 600 W at 40 kV.

2.1.2 Battery stack

The design requirements of the battery stack specifically are to be able to provide a maximum power output of 700 W continuously for 1 minute or more at a nominal voltage of approximately 200 V. The power requirement reflects the highest power of the possible configurations of the EAD aircraft, incorporating an anticipated power conversion efficiency of approximately 85%. The voltage requirement is determined by the input side of the power converter. For less power intensive designs of the aircraft, the reduced consumption is reflected as increased flight time between charges. The battery stack produces heat as it discharges, and this heat must not interfere with the other components of the power system.

Six cell pack design

The battery stack is made from E-flite 150 mAh 45 C lithium polymer battery cells, which were chosen after demonstrating a power density of 4.3 kW/kg, the highest among several cells tested.

Packs of six cells in series were created as modular portions of the full battery stack that can be charged individually and replaced if damaged. To reduce weight and complexity, balancing wiring and plugs were not included. This will reduce the number of achievable charge cycles and limit charging rates, but these are not primary concerns for the aircraft flight tests. However, in an effort to reduce cell imbalance, each cell's internal resistance was measured and k-means clustering was used to find groups of cells of least variation in internal resistance. The internal

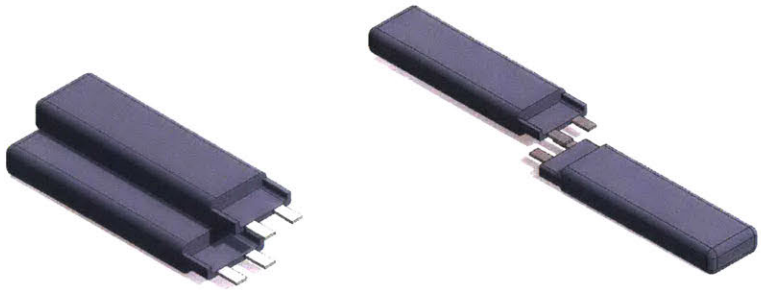

Figure 2-1: Two options for stacking individual cells into packs.

resistance was measured by discharging at different currents (0.75 A and 1.5 A) and using the relationship $\Delta V = \Delta I R_{\text{internal}}$, where ΔI is the difference between two discharge currents (A), ΔV is the difference in voltage that the battery supplies between the two current levels (V), and R_{internal} is the battery cell's internal resistance.

Assuming constant capacity across all cells, reducing variation in internal resistance results in reducing variation in cell voltage throughout a charge or discharge, which minimizes the possibility of a particular cell within a pack of going outside its operating voltage range and becoming damaged. The operating voltage range for lithium polymer battery cells is typically 3.0 to 4.2 V.

The cells come with small pluggable connectors but in order to reduce ohmic losses through them, these were removed and leads were soldered together when connecting them in series. The two options that were considered in terms of arranging the cells into larger packs are shown in Figure 2-1. The leads of many cells were too short for the arrangement shown on the left so the arrangement on the right was chosen despite it being potentially less mechanically robust.

The resulting six-cell pack configuration is shown in Figure 2-2. To improve strength and provide electrical insulation, the leads were covered in a layer of epoxy. A positive and a negative lead are attached to the ends of the pack and Deans Micro Plugs are used for their compactness, low resistance, and low weight.

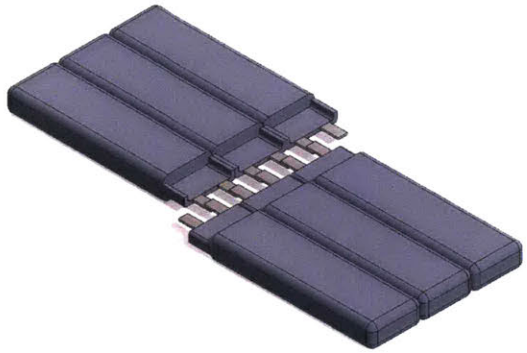

Figure 2-2: A modular six-cell battery pack.

Full stack design

The full battery stack is composed of several six-cell packs operating in series and is shown in Figure 2-3. Up to nine packs can be used to bring the nominal discharge voltage of the full stack to ~200 V.

Figure 2-3: Packs of six are wired in series to produce a full battery stack.

A compact arrangement like this will allow the battery weight to be placed far forward in the nosecone as shown in Figure 2-4. The battery and power converter mass together make up approximately 40% overall aircraft mass and their exact position can be adjusted to place the airframe's center of mass in the desired location of approximately 30% of of the chord length behind the leading edge of the wing, in

which condition the aircraft is designed to be stable.

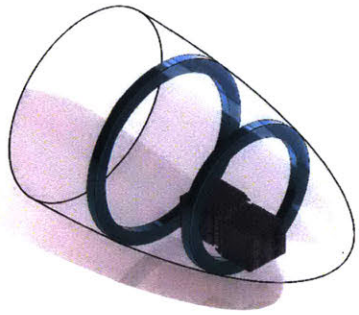

Figure 2-4: The battery stack is placed in the nosecone and it can be moved to adjust the position of the airframe's center of mass.

2.1.3 High voltage power converter

The power converter is a DC-DC converter where the main objective of its development was to produce a high voltage converter with higher specific power (kW/kg) than commercially available. The design goal is to produce a converter capable of 600 W at 40 kV output, at a mass of 550 g.

The power converter is put into standby mode by a physical switch, at which point a power-on signal from the RC controller initiates the start sequence of the high voltage side. The power converter reaches the high voltage setpoint and maintains it until it receives the throttle-off signal from the RC controller, unless any fault conditions are met. The faults monitored are battery side low voltage, battery high temperature, maximum thrust-on timer, and maximum current. The implementation of the communication with the power converter is discussed in more detail in Section 2.2.1.

The output side must be able to ramp the voltage from 0 to 40 kV over approximately 20 s, and hold at 40 kV until shut off. The ramp was required after testing with the thrusters revealed that turning the high voltage on immediately resulted

in streamer formation and increased the risk of arcing. Streamers are areas of higher current relative to the rest of the thruster, and are precursors to arcing. When they do not result in arcing, they still draw more power than normal operation and are therefore undesireable. The approximately 20 s ramp alleviated this issue. The thrusters are discussed in more detail in the following section.

2.1.4 Thrusters

A thruster consists of an asymmetric electrode pair. The forward electrode is by design smaller than the rear electrode, so that the stronger resulting electric fields near this forward electrode are able to ionize the air surrounding it. The ions are then accelerated to the rear electrode and transfer momentum to the surrounding air, and therefore create thrust. The forward electrode is referred to as the emitter and the rear electrode is referred to as the collector.

Design point

A summary of the thruster design point for the powered flights that were performed in July of 2017 is given in Table 2.1. Note that maximum field strength E_{max} is not the maximum physical field strength but the average given by V/d.

Table 2.1: Design point specifications for powered flight testing in July 2017.

Variable Name	Symbol	Value
Maximum voltage	V_{max}	40 kV
Gap distance	d	5 cm
Maximum field strength	E_{max}	8.0×10^5 V/m
Thrust per length	T/L_{th}	0.094 N/m
Total thrust	T	2.47 N

The thrusters are arranged into two stages of 3 emitter/collector pairs, at a length of 4.4 m each. The emitter is a 32 AWG stainless steel wire, and the collector is a NACA 0010 airfoil with a chord length of 5.08 cm (2 inches) and made of a foam core with the forward portion of the airfoil covered with a layer of aluminum tape. A cross-section is shown in Figure 2-5.

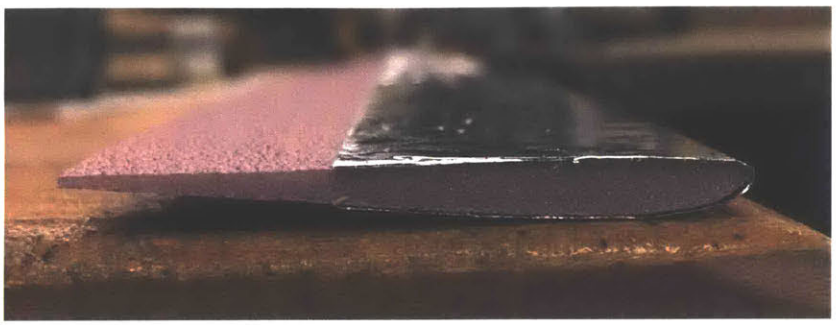

Figure 2-5: Cross section of a collector.

Issues and alternative designs

Wrinkles and tears in the aluminum tape are the primary practical concern with this design, especially when approaching maximum operating voltage. These surface features concentrate the electric field at the collector, encouraging streamer formation, which as noted before are power sinks. The surface imperfections can also ionize air at the collector, creating a reverse direction ion flow, which reduces thrust and increases power. Both of these phenomenon also lead to arcing. A secondary difficulty with the aluminum tape arises when the tape separates from the foam airfoil profile and thereby causing an increase in drag. Together, these tend to make this design have a short working lifetime and collector manufacturing is a time-intensive task.

Table 2.2: Proposed modifications to collector design and associated drawbacks.

Substitute in	Substitute out	Drawback
Carbon fiber cloth	Aluminum	Increased streamer formation
Conductive paint	Aluminum	Cracks
3D printed lattice	Foam airfoil profile	Weight
Electroplating	Aluminum	Weight of substrate

In order to mitigate these issues related to the aluminum surface imperfections, some design modifications relative to Gilmore [10] were tested and are given in Table 2.2, together with the associated drawback that inhibits their use. Another possible solution is to use a doped, electrically conductive polymer tape which would be less prone to wrinkles than aluminum, but a suitable, commercially available polymer tape has not yet been tested.

Having described the design of the three major components of the power system (the batteries, HVPC, and thrusters), the next section details the communication system, which is used to control the power system as well as control the motion of the aircraft.

2.2 Communication system

Communication to the aircraft's control system is through a standard RC airplane transmitter and receiver system. Two remote pilots share responsibility of flying the aircraft. One is given control over steering and the other controls the power switch, which turns on the thrusters. If a fault is detected on board the power is cut automatically by the power converter. All other logic necessary to control the thrusters during flight is accomplished by a closed-loop voltage control circuit on the high voltage power converter. A schematic of the electrical and communication system is shown in Figure 2-6.

Transmitter

The thumbsticks of one transmitter are used to steer the aircraft by controlling the tail rudder and elevator. The other transmitter controls the power with a switch.

Receiver

Two Spektrum AR6310 receivers are implemented on the aircraft to receive the signals from the transmitters. One receiver is placed on the tail and directly controls two servos, one for the rudder and one for the elevator. The other receiver is placed in the nosecone and generates the power switch signal which is given to the high voltage power converter. Only one receiver is required for these tasks, but due to the distance between the tail and HVPC, two receivers are used to reduce weight compared to running wires between the two locations. The receivers' operating voltage range is 3.5 V to 9.6 V, which allows the use of single-cell lithium polymer batteries to power them.

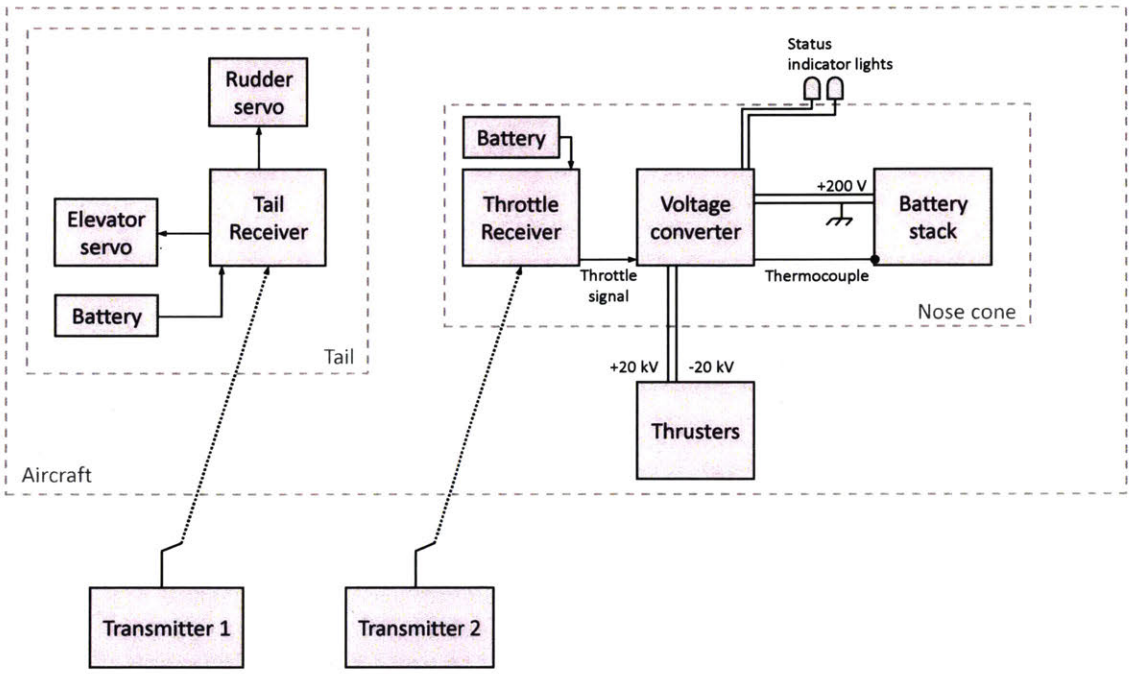

Figure 2-6: Schematic of the electrical and communication system. One transmitter controls the servos on the tail to steer the aircraft and one transmitter controls the power switch. A single cell battery powers each receiver and LEDs indicate the status of the power system.

Table 2.3: Attributes of the power switch signal.

Attribute	Value
Pulse magnitude	3.12 V
Power "off" pulse duration	1.10 ms
Power "on" pulse duration	1.94 ms
Signal period	22.0 ms

Servo

Dymond D47 power servos are used to move the rudder and elevator. The servo can supply a holding torque of 0.14 Nm, which is sufficient to hold expected loads on the tail surfaces.

2.2.1 Power switch signal

A typical RC airplane's throttle will be controlled through the up/down motion of the left thumbstick, which gives a continuous 0-100% signal to an electronic speed controller. But since we need only on/off functionality of our thrusters, the "gear" switch on the transmitter is used, which is typically intended for any on/off auxiliary system command such as landing gear up or down.

Two wires, chassis common and signal high, are given to the high voltage power converter which directly controls the thruster output. The power switch signal is a PWM wave and the width of the signal is read by the control board of the power converter and interpreted as either thruster-on or thruster-off. Measurements with an oscilloscope found attributes of the power switch signal, which are given in Table 2.3.

In order to decode the signal for use on the power converter, measurements were made with an oscilloscope. The receiver was found to generate a pulse-width-modulated (PWM) signal with attributes given in Table 2.3. The power converter reads this PWM signal and turns the thrusters on if the pulse duration is greater than 1.5 ms, and turns the thrusters off otherwise.

2.2.2 Range and loss of communication

Spektrum does not cite a usable range for their devices other than by classifying them as "park flyer", partly because many factors affect the connection quality. However, the connection was tested to work over hundreds of meters and through building walls, as noted in Section 3.2, which is considered sufficient for the planned flight tests.

If communication is lost between the transmitter and receiver, the receiver is programmed to turn the thrusters off and command neutral rudder and elevator positions.

2.2.3 Power source and current draw

A single cell battery powers the receiver on the tail, which powers the two Dymond D47 servos connected to it to move the rudder and elevator. The servos each draw a maximum of 250 mA, to total 500 mA required from the battery cell at maximum load. A West Mountain Radio CBA IV is used to discharge a battery cell at constant current to find that under these conditions, a cell will provide power for at least 13 minutes before the voltage drops below 3.5 V.

2.3 Aircraft structure

This section describes work done on the aircraft wing and tail. For the wing, the process to find an airfoil that would improve the wing performance is described. Then a full design process is presented for the tail.

2.3.1 Wing airfoil refinement

An airfoil optimization for the main wing was undertaken and is presented here. The design Reynolds number is 100,000 (or ~4.7 m/s) and the wing incorporates a main, straight lifting section and at the ends, shorter sections with dihedral. It has constant chord and no taper, which simplify manufacturing. The dihedral sections

Table 2.4: L/D of three candidate airfoils near the design $C_L \approx 1$.

Airfoil name	$C_L = 0.8$	$C_L = 1.0$	$C_L = 1.2$
asv02	24.3	23.5	18.2
tS12	24.0	21.9	18.1
Aquilasm	23.0	21.5	19.3

add roll stability, allow the aircraft to roll into turns without the use of ailerons, and reduce induced drag. These design choices were left unchanged, but the airfoil that the wing was based on was modified from Gilmore [10].

The University of Illinois' Airfoil Coordinate Database [13] was used to identify several candidate airfoils that are designed to achieve high lift to drag at low Reynolds numbers. The airfoil coordinates were imported into XFOIL [14] to estimate the L/D performance at Re $= 1 \times 10^5$ near the design $C_L \approx 1$. The performance of three candidate airfoils are given in Table 2.4.

The asv02 achieves the highest L/D, but the performance is more dependent on C_L than the other airfoils. The tS12 and the Aquilasm perform similarly, but the Aquilasm achieves the most constant L/D over the range of C_L and for this reason is chosen to make the aircraft performance more predictable and to reduce the risk of reduced performance if the realized C_L in flight testing is different than predicted.

The other aerodynamic element of the aircraft that is presented in this thesis is the tail, which is discussed in the following section.

2.3.2 Tail

Testing of an earlier version of the aircraft found that the rudder and elevator were both unable to control the aircraft's yaw and pitch, respectively. In order to correct for this, a new tail was designed and manufactured, and the design process is given here. The variables used in this analysis are defined in Table 2.5 and illustrated in Figure 2-7.

Table 2.5: Variable definitions for this tail design analysis.

x	Distance from wing leading edge	AR_v	Vertical tail aspect ratio
S	Wing planform area	l_h	Horizontal tail moment arm
S_h	Horizontal tail planform area	l_v	Vertical tail moment arm
S_v	Vertical tail planform area	V_h	Horizontal tail volume coefficient
b	Wing span	V_v	Vertical tail volume coefficient
c	Average chord of main wing	C_L	Coefficient of lift
AR	Wing aspect ratio	α	Angle of attack of main wing
AR_h	Horizontal tail aspect ratio		

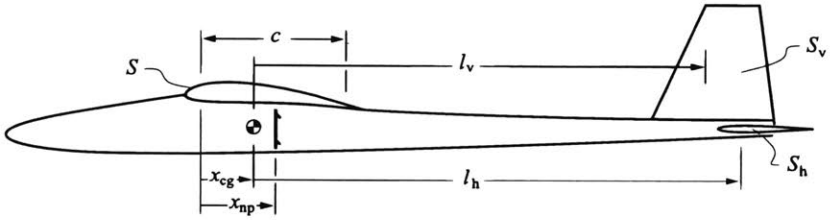

Figure 2-7: Variable definitions for tail analysis. Figure from MIT OpenCourseWare [15].

Tail design changes summary

Attributes of the previous tail as well as the refined tail are presented here first in Table 2.6 and the design process follows. All dimensions are measured from the wing leading edge (positive toward tail). The length dimension of the Reynolds number is based on average chord of the respective wing. Total tail mass includes the entire tail, servos and related hardware, RC receiver, and a single cell battery.

Shape and construction

A conventional fuselage mounted tail is selected for ease of manufacturing, mounting to the aircraft, and control. This layout has only one structural connection for all tail surfaces to the aircraft tail boom (similar to a V layout but unlike a T or H layout, for example), which simplifies the tail design and mounting connections and is most likely be the lightest of the configurations. Since it has one vertical surface and one horizontal surface, the rudder and elevator controls are decoupled. Other considerations such as recovery from stall are not applicable here.

A detailed analysis is not performed to optimize the aspect ratio of the tail surfaces

Table 2.6: Summary of previous tail and refined tail attributes with major changes bolded.

	Previous tail [10]	Refined tail
AR_h	4.0	4.0
AR_v	2.4	2.5
S_h	0.13 m^2	0.13 m^2
S_v	0.052 m^2	**0.077** m^2
V_h	0.39	0.40
V_v	0.014	**0.020**
$Airfoil_h$	Symmetric, 8% thickness	**NACA 0008**
$Airfoil_v$	NACA 0012	**NACA 0008**
Re_h	53100	53500
Re_v	43600	52300
l_h	1.40 m	1.40 m
l_v	1.40 m	1.40 m
x_{cg}	0.101 m	0.101 m
x_{np}	0.194 m	0.194 m
SM	0.28	.028
m_{total}	110 g	**85** g

because aspect ratio does not heavily influence the performance of a lightly-loaded tail. However, a survey of sailplane gliders shows tail aspect ratios in the range of 2 to 5, with vertical surfaces tending to the lower end and horizontal surfaces toward the higher end.

The tail is designed for a low speed vehicle (Mach number $\ll 1$) so sweep is unnecessary. However, for aesthetic reasons the leading edge of each tail surface is swept back 10° and the trailing edge is kept perpendicular to the aircraft's axis.

Since the direction of tail loading may be in any direction while controlling the aircraft, a symmetric airfoil is chosen. The aircraft is not designed to be highly maneuverable so the tail does not have to reach high lift coefficients before stall and therefore a thin airfoil is beneficial in order to reduce pressure drag. Therefore, a NACA 0008 airfoil is chosen as the basis of both vertical and horizontal tail surfaces. The tail is made of Owens-Corning R10 insulation foam.

Sizing

Volume coefficients are used to determine how large the tail surfaces should be, and are defined as

$$V_h = \frac{S_h l_h}{Sc} \tag{2.1}$$

$$V_v = \frac{S_v l_v}{Sb}. \tag{2.2}$$

The horizontal volume coefficient plays a role in aircraft stability and pitch control while the vertical volume coefficient determines the yaw stability and control. Drela et al. [15] recommends coefficients in the ranges $0.30<V_h<0.60$ and $0.02<V_v<0.05$ and Raymer [16] recommends specifically for sailplanes V_h=0.5 and V_v=0.02. The previous tail design had $V_v = 0.014$, which accounts for poor yaw control noted during testing. The new tail design leaves the horizontal coefficient unchanged and increases the vertical coefficient from 0.014 to 0.020 by increasing the vertical tail planform size.

Stability

After having determined the geometric properties of the tail, we find the neutral point of the aircraft and place the center of gravity (cg) in a position that will produce a dynamically stable aircraft.

In order for the aircraft to be stable in pitch, the cg must be placed ahead of the neutral point [16]. The location of the neutral point h_n estimated by

$$h_n = \frac{h_{\text{nw}} + h_h \eta_t \frac{S_h a_h}{S a_w}(1-\epsilon_\alpha) + \frac{C_{M,\text{body}_\alpha}}{a_w}}{1 + \eta_t \frac{S_h a_h}{S a_w}(1-\epsilon_\alpha)}, \tag{2.3}$$

where a description of all previously undefined variables and assumptions are provided in Table 2.7. All variables denoted with an h are distance measured from the wing leading edge, expressed in multiples of the wing chord. The aerodynamic center of the wing is taken as the quarter chord location. The free stream dynamic pressure at the tail is assumed to be the same as at the wing and the effect of moments

Table 2.7: All previously undefined variables that are used in the stability and moment analysis. BL denotes boundary layer.

Variable	Value	Units	Description
h_{nw}	0.250	-	Aerodynamic center of main wing
h_h	4.473	-	Horizontal tail moment arm to aircraft cg
η_t	1	-	Multiple of free stream dynamic pressure at the tail
a_w	0.088	1/°	Slope of C_L vs α of main wing (Re=1 $\times$ 10^5 and α=8°)
a_h	0.041	1/°	Slope of C_L vs α of horiz. tail (Re=5.4 $\times$ 10^4 and α=0°)
$a_{h,\text{tripped}}$	0.106	1/°	Slope of C_L vs α of horizontal tail with turbulent BLs
ϵ_α	0.262	°/°	Slope of downwash angle vs α
C_{M,body_α}	0	-	Slope of C_M vs α for all other body components

due to other components such as the fuselage are neglected (only the wing, tail, and cg are considered). The effects of downwash are described in Section 2.3.2.

The slope of the lift coefficient vs angle of attack for the wing, a_w, is found from XFOIL using the design angle of attack of 8° and design Reynolds number of 1×10^5. The same is done for the refined horizontal tail section near an angle of attack of 0° and its design Reynolds number of 5.35×10^4. This is also calculated for the horizontal tail when its boundary layers are tripped to turbulence at the leading edge.

The slope of C_L vs angle of attack for the horizontal tail depends on whether the boundary layers are laminar or turbulent, and therefore the location of the neutral point of the aircraft also depends on this. Because the Reynolds number is around the transition region, both cases are considered for finding the neutral point of the aircraft. The stability margin is defined as

$$\text{SM} = h_n - h_{\text{cg}} = \frac{x_h - x_{\text{cg}}}{c}. \tag{2.4}$$

In order to achieve a stable aircraft the stability margin must be positive and $0.05 < \text{SM} < 0.15$ is recommended, although more strongly stable aircraft may have higher stability margin [15]. Excessive SM diminishes the aircraft maneuverability and requires rudder trim adjust upon speed change, but we favor higher SM values for this aircraft since we prioritize stability over maneuverability and there is only one design speed. If the cg is placed at 30% of the wing chord the stability margin

Figure 2-8: Pitching moment diagram.

predicted by this analysis is $0.085 < \text{SM} < 0.281$, where the lower bound corresponds to laminar flow over the tail and the upper bound to turbulent flow. The calculation done is only an estimate and adjustments can be made by moving the cg if testing shows inadequate stability. The turbulent value is used since the tail surface is not smooth.

Moment analysis

A pitching moment analysis about the aircraft cg is performed in order to find the required lift coefficient of the tail for aircraft trim. This is then used to choose the angle of attack the tail is mounted with. Thrust force is neglected because it acts near the cg and is much smaller than the lifting forces (the lift to drag ratio of the aircraft with the thrusters mounted and unenergized is estimated to be near 10). A diagram for the moment calculation is shown in Figure 2-8. Setting the sum of the moments about the cg equal to zero yeilds

$$(x_{\text{cg}} - x_{\text{nw}})L + M - l_h L_{\text{tail}} + M_{\text{tail}} + y_{\text{drag}} D = 0. \tag{2.5}$$

XFOIL is used for estimating $L, M, D, L_{\text{tail}}, M_{\text{tail}}$ and to show that $M_{\text{tail}} \ll l_h L_{\text{tail}}$ over a tail angle of attack range of -15 to 15°. This then constrains the tail lift and aerodynamic angle of attack required for trim.

Placing the cg at 30% wing cord results in a near-zero, positive lift that the tail must provide, which has the benefit of not creating any downward force that the wing must counteract, increasing induced drag.

Downwash

The vortex system of the main wing produces a downward velocity component that the tail experiences, and we adopt an approximate method to estimate the downwash angle ϵ.

The wing is approximated as a bound vortex which spans b' with circulation Γ_0 where this circulation is constrained by the lift and inviscid theory gives $\rho v \Gamma_0 b' = \frac{1}{2}\rho v^2 S C_L$. This is used instead of the full wingspan because as the vortex sheet leaves the aircraft it forms two vortices separated by b'. We are left with estimating b' and take the analytic solution for an elliptic wing: $b' = \frac{\pi b}{4}$.

The Biot-Savart law is used to find the induced downward air velocity w at the tail created by a straight-line vortex. After this analysis, the downwash angle is found to be $\epsilon = 3.4°$, which is used when mounting the tail to the aircraft. Ground effect is not considered here.

2.4 Launcher

The aircraft is not capable of takeoff under its own power, so a launcher is used to accelerate the aircraft to at least its nominal flight speed and altitude of ~5 m/s and $1 - 2$ m above the ground. A rigid frame supports a slide constructed from 80/20 extruded aluminum framing, and a cart is able to move relative to the slide via roller bearing wheels. The aircraft is placed on the cart and attached to it with a small printed hook, and the cart and airframe together are accelerated through the launch process under the influence of a tug rope and large spring element. As the end of the runway is approached, a second rope and spring element decelerate the cart and the aircraft is launched. Figure 2-9 illustrates the system.

2.4.1 Energy requirements

A consideration of the design is to reduce the launch loads imposed on the airframe during the launch process, since requiring more strength of the airframe constrains

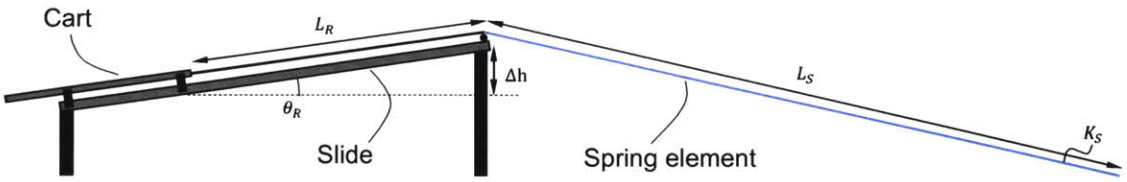

Figure 2-9: Schematic of the launcher with relevant variables.

the design to add strength and mass where otherwise unnecessary. This translates into increasing the runway length and increasing the length of the spring element used. The former reduces average required acceleration and the latter reduces peak acceleration.

An energy-based model is created to predict how much energy must be stored in the spring element in order to launch the aircraft. The energies considered are

$$E_{\text{kin}} = 1/2(m + m_{\text{cart}} + m_{\text{rope}})v_{\text{launch}}^2, \tag{2.6}$$

$$E_{\text{pot}} = (m + m_{\text{cart}})g\Delta h, \tag{2.7}$$

$$E_{\text{slide}} = F_{\text{slide}}L_R, \tag{2.8}$$

$$E_{\text{spring}} = E_{\text{kin}} + E_{\text{pot}} + E_{\text{slide}} = 1/2\left(K_S\left({e_2}^2 - {e_1}^2\right)\right), \tag{2.9}$$

where m is the aircraft mass, m_{cart} is the cart mass, m_{rope} is the tug rope mass, v_{launch} is the launch velocity, F_{slide} is the friction between the slide and rail, K_S is the spring constant of the spring element, and

$$e_2 = L_S - L_0, \tag{2.10}$$

$$e_1 = (L_S - L_R) - L_0, \tag{2.11}$$

where L_S is the spring's stretched length, L_0 is the spring's unstretched length, and L_R is the runway length. The energy stored in the spring between lengths e_2 and e_1 is set equal to the other three energies, since it must provide all of the energy transferred during the launch process. Table 2.8 gives parameters of the launcher system design.

Table 2.8: Final parameters of the launcher system design.

Parameter	Value
Launch velocity	5 m/s
Maximum acceleration	1.25 g
Spring length, stretched	9.9 m
Spring length, unstretched	3.7 m
Runway length	2.1 m
Spring constant	20 N/m
Slide friction	35 N

2.4.2 Front carraige and electrical isolation

In order to allow the aircraft thrusters to reach full voltage before leaving the launcher, the aircraft cannot touch anything conductive and must have an appropriate separation from any conductive parts to ensure that no ion flows are directed toward the launcher.

The front carriage of the launcher is the front portion of the sliding cart and bears most of the loads of the launch. It is shown in Figure 2-10, which highlights the bottom strength plate, the metal wheels, the electrical spacer for thruster operation, and the top plate with the pocket where the hook on the aircraft is anchored. Testing without the bottom strength plate showed that the axles that the wheels sit on would bend outward after several launch sequences, so the strength plate was added to stop this.

The electrical spacer is constructed from 1.27 cm (0.5 in) thick ABS plastic and all joints are created as mill pockets before being joined by an appropriate plastic cement. Its height is such that the aircraft is kept 25 cm (5 times the electrode gap spacing) away from any conductive materials on the launcher. Also can be seen are the areas where the front tug rope and the decelerating arresting rope are attached to the front carriage.

(a) Side view.

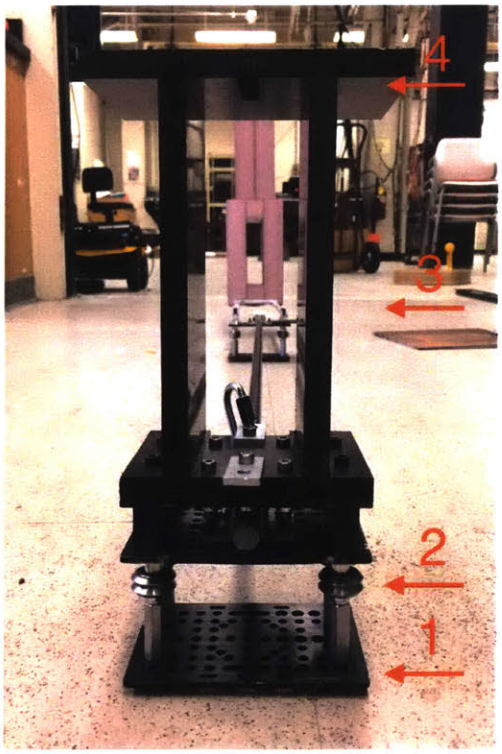

(b) Front view.

Figure 2-10: Launcher front carriage. Items labeled in the front view include 1) bottom strength plate, 2) metal roller wheels, 3) electrical spacer, 4) top plate with hook pocket.

Chapter 3

Subsystem testing and verification

This chapter presents the testing that took place in preparation for flight tests. The power system is presented first starting with the the battery stack, then test results for the power converter and thrusters, as well as results with the full power system functioning with the battery stack, HVPC, and airframe thrusters functioning together. The communication system is then shown to function as expected in proximity of the thrusters being powered by high voltage. After this, the airframe propeller tests are described in relation to the aerodynamic behavior of the system with the new wing airfoil and tail. The launcher also undergoes launch testing to ensure reliability of the system, and electrical isolation testing to ensure the aircraft can be powered on while on the launcher.

3.1 Power system

The battery stack, HVPC, and thrusters are first tested individually, then integrated testing is performed where these components are connected together. The electrical and thermal tests of the battery are presented first.

3.1.1 Battery stack electrical testing

The battery stack is designed to provide up to 700 W (~600 W delivered to thrusters) at approximately 200 V for at least 1 minute. Though flight tests are performed at a lower power level, individual subsystem tests are performed up to the design point of 700 W to ensure any future iterations on the vehicle do not require major revisions in the subsystems.

Test equipment

The six-cell packs are individually charged with the Hitec X4 Multi Charger AC Plus. They are charged at 0.2 A (1.33 C) to 25.2 V (4.2 V per cell) shortly before use, and taken to a storage voltage of 22.8 V (3.8 V per cell) at all other times.

A B&K Precision model 8616 programmable DC electronic load provides the load for all discharge tests. Constant power discharge mode is used to simulate the high voltage power converter.

Individual pack electrical test results

Figure 3-1 shows the time each battery pack can sustain until it is drained. Several discharge power levels, where the highest level of 80 W per pack corresponds to 720 W from a full battery stack if nine packs are used. All tests end when the average cell voltage (while discharging) drops to 3.2 V. We see that at least 80 seconds is attainable for the highest discharge rate, and discharge time on the order of several minutes can be sustained for the lower power levels.

A typical discharge curve for a single pack is shown in Figure 3-2 and shows the relatively steep voltage gradient that the batteries exhibit at the beginning of a constant-power discharge, which has implications on the control system implemented in the power converter.

Typical discharge curves are shown for a single six-cell pack for various discharge rates in Figure 3-3. As more power is required from a pack, the voltage at which it delivers current decreases. This trade off constrains the full battery stack to a

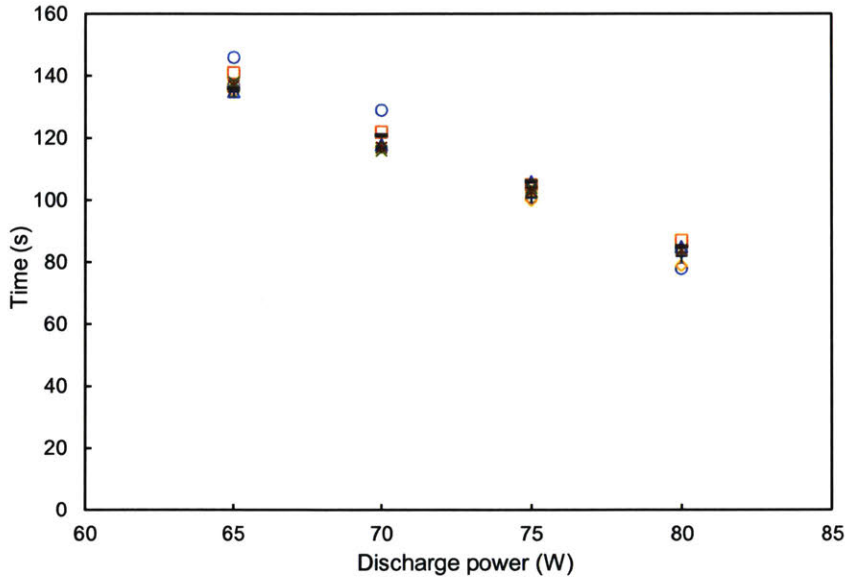

Figure 3-1: Time that the individual battery packs can deliver power until empty for various power delivery levels. The different markers represent different battery packs.

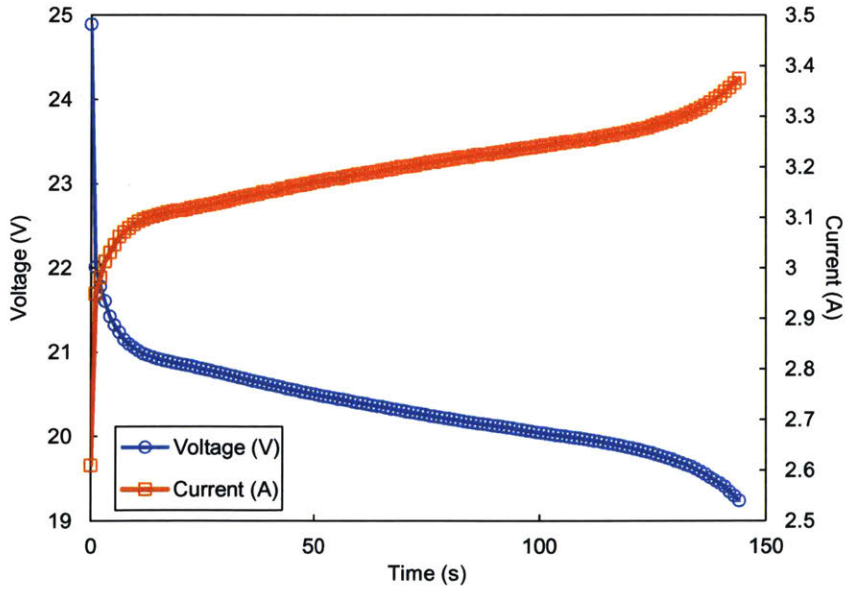

Figure 3-2: A typical discharge curve of a single pack when delivering constant power (65 W in this example).

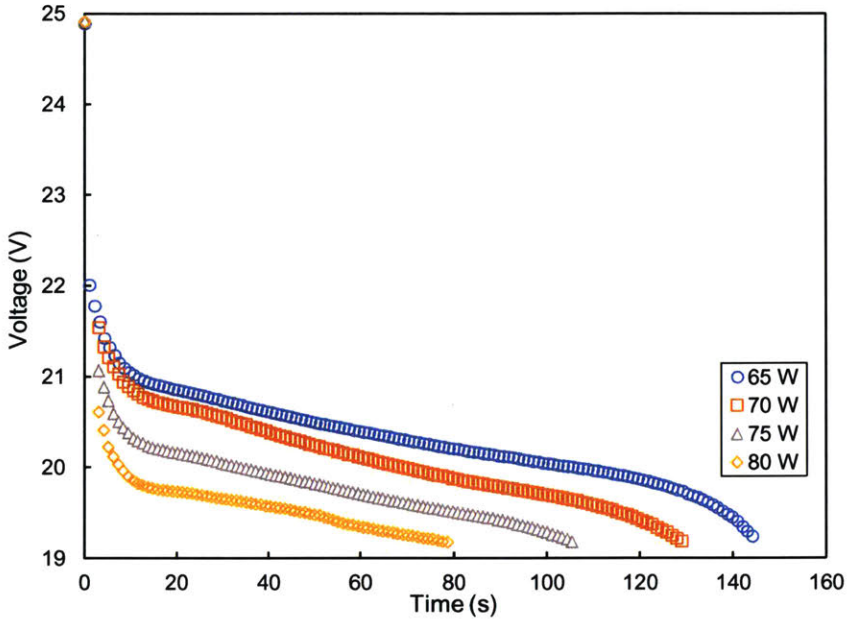

Figure 3-3: A single battery pack shows lower nominal discharge voltage as discharge power is increased.

minimum of eight packs due to a minimum required input voltage to the power converter of 160 V.

Full stack electrical test results

Just as in the individual pack discharge tests, the full stack was discharged at constant power and each discharge ended when an average cell voltage of 3.2 V was reached. Nine packs of six cells were connected in series and laid out on the lab bench when discharged. After performance was verified when connected in series, the packs were then arranged into a stacked configuration and thermal tests were run.

Since the highest required power is 700 W and the packs have been shown to work individually up to this maximum, only the two discharge rates 675 W and 720 W were tested. These rates were selected to be consistent with the highest single pack discharge rates (75 W and 80 W, respectively).

Figure 3-4 shows the discharge test results. Power delivery lasted for 130 s and 123 s for the two tests, which are both longer than the corresponding tests for any of the single pack discharges (~100 s and ~85 s, respectively). An explanation for this

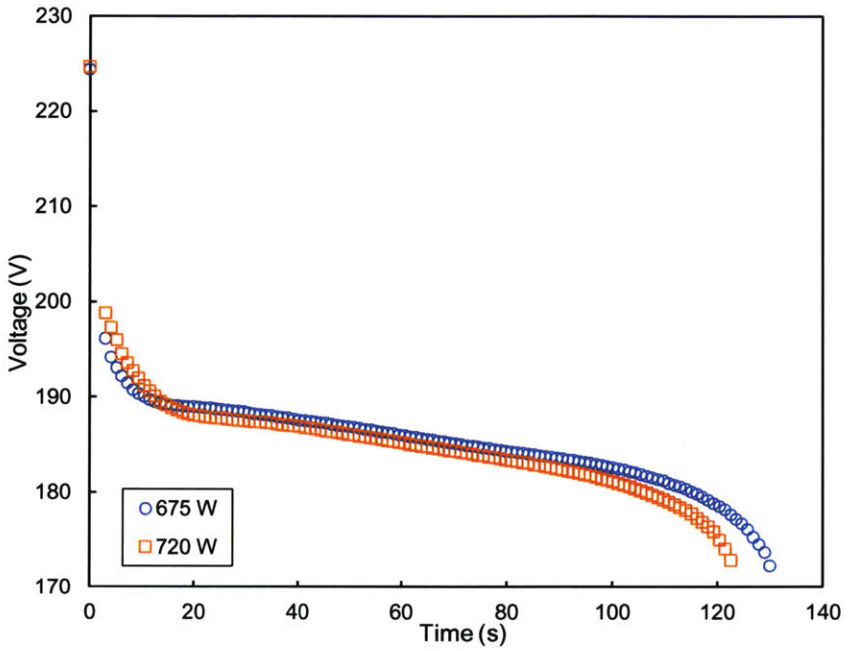

Figure 3-4: Full stack of nine battery packs discharge performance at highest required powers.

discrepancy may be some unaccounted for line resistance in the discharge setup (the effect of which would be decreased when testing with more battery packs).

3.1.2 Battery stack thermal testing

The battery stack heats up while it discharges and can be damaged by excessive temperature. The thermal behavior of the battery packs are evaluated to answer whether achievable flight time is limited by battery capacity or battery temperature. If planned discharge rates cause the battery temperatures to exceed a certain threshold, temperature sensing must be implemented on the aircraft control logic to avoid thermal damage to the batteries.

Temperature of the batteries is recorded during discharge tests both on the individual packs and on the full battery stack. When the packs are discharged individually, show that a maximum of 55 °C cell temperature can be expected at the highest discharge power, which is below the stated maximum of 65 °C for the E-flite cells and is also safe for all materials used in the fuselage. Temperature is monitored as the packs

cool down after a discharge and results in a thermal time constant of approximately 5 minutes.

When the battery packs are arranged into a stack, discharge rates of 60 to 80 W per pack cause the batteries to reach the maximum 65 °C before being depleted, necessitating the use of a thermocouple on the aircraft. In this configuration, a thermal time constant of approximately 11 minutes is found.

Test equipment

Three K-type thermocouples are used for all thermal testing in conjunction with amplifiers based on the Analog Devices AD8495 amplifier chip (adafruit product ID 1778). Signals were then recorded with LabVIEW and a National Instruments USB-6009 data acquisition device. The voltage measurement precision of the USB-6009 results in a precision of ± 2 °C of the temperature measurements. A FLIR thermal camera is used for identifying hot spots and qualitatively assessing thermal behavior.

Individual pack thermal test results

Temperature measurements were also recorded by the thermocouples and thermal images were taken. The thermal images reported $5 - 10$ °C higher than the thermocouples. Due to unknown thermal emissivity of the battery packs' outer material, the value of the temperature reported by thermal images is not used, but the spatial variation they show is useful to find hot spots on the cells, and none were found as seen in Figure 3-6. Figure 3-5 shows that the thermal behavior is consistent throughout the different packs.

Figure 3-7 shows the cool down behavior of individual packs in ambient air. We note that a complete discharge is on the order of 1-2 minutes while a complete cool down takes longer, exhibiting a time constant of approximately 5 minutes.

Full stack thermal test results

Thermal tests are conducted where multiple packs are discharged together in order to determine if the batteries may be stacked on top of each other in a compact ar-

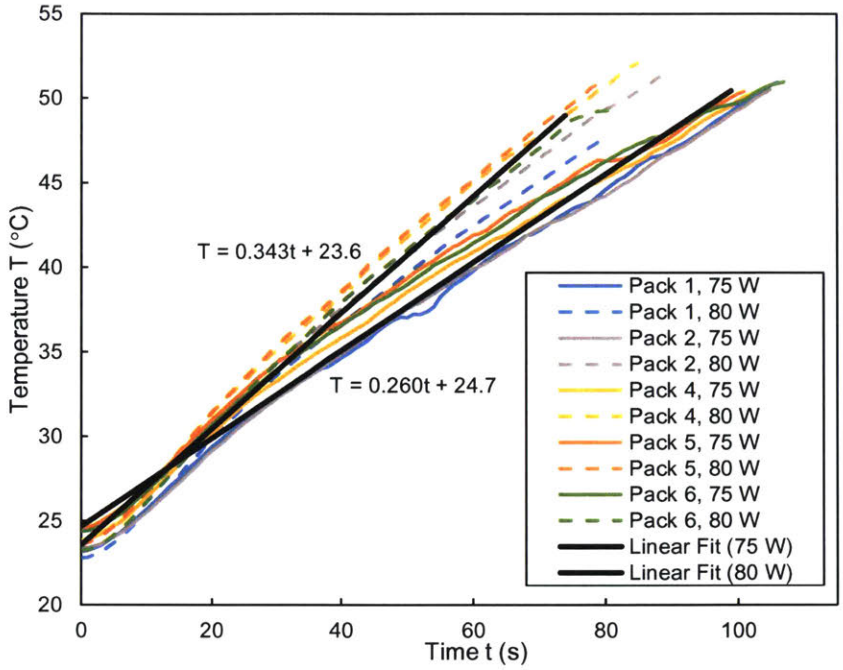

Figure 3-5: Individual battery pack thermal behavior for high discharge rates. Packs show approximately linear temperature increase in time and behavior is consistent across packs.

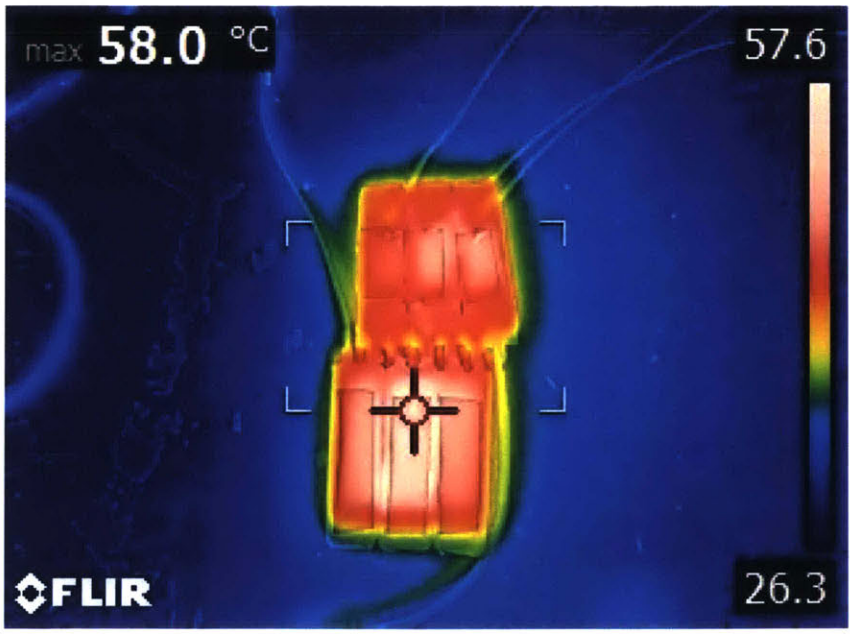

Figure 3-6: Thermal image of a single pack at end of discharge.

rangement or if they must be physically separated to reduce maximum temperatures. Four packs were stacked and thermocouples were placed in between the middle two,

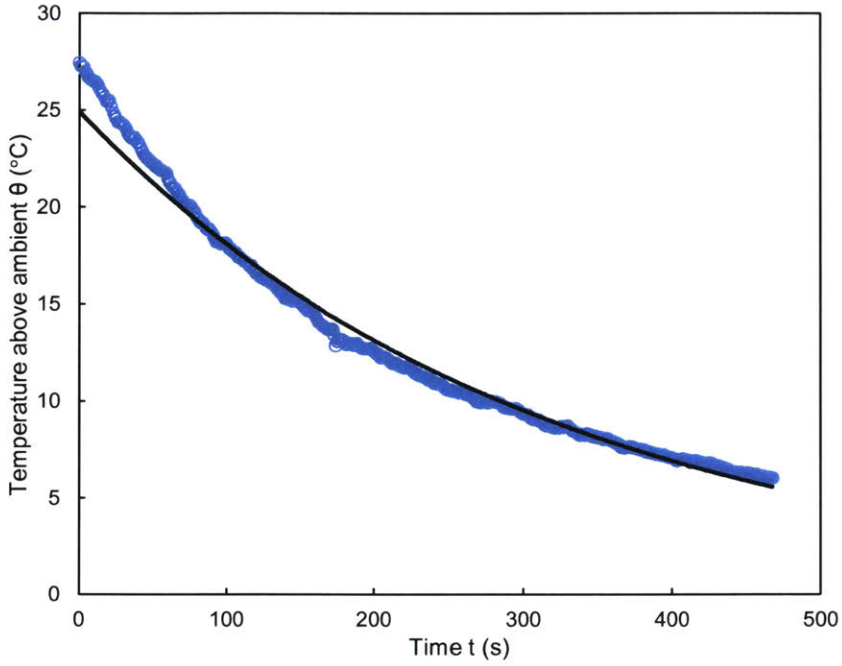

Figure 3-7: Single pack cool down. The black line is an exponential fit $\theta = 25\exp(-t/299)$ where θ is °C above ambient, and t is in seconds.

as shown in Figure 3-8. The temperature measurements are shown in Figure 3-9.

Similarly to the single pack tests, a linear relationship between temperature and discharge time is exhibited. An result is seen that when the packs are stacked on top of each other, the thermal resistance to the environment is increased sufficiently such that for the higher discharge rates (60 to 80 W per pack), the time of power delivery is limited by temperature rather than battery capacity, since tests were not allowed to continue above 65 °C which would damage the batteries. The lower discharge rates (40 to 50 W per pack), on the other hand, do not reach a high temperature but rather reach the end of test due to cell capacity.

This result forces the control strategy of the power converter to determine end-of-test not only by user input and cell voltage level, but it must also consider temperature. Another K-type thermocouple is implemented in the power converter to detect a high battery temperature event (set to 60 °C) and turn off the thrusters.

For comparison, at the most demanding design discharge rate of 80 W per pack, which corresponds to over 600 W delivered power to the thrusters for a complete

Figure 3-8: Experimental setup for inner-stack temperature measurement with thermocouples.

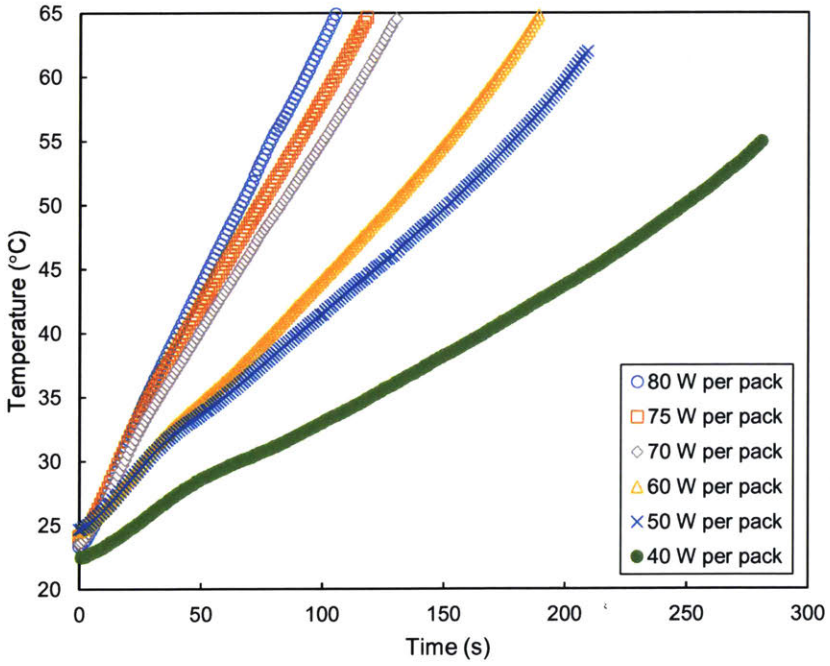

Figure 3-9: Inner stack battery temperature throughout discharge for multiple discharge rates. Higher power tests are ended due to high temperature while lower power tests are ended due to battery capacity.

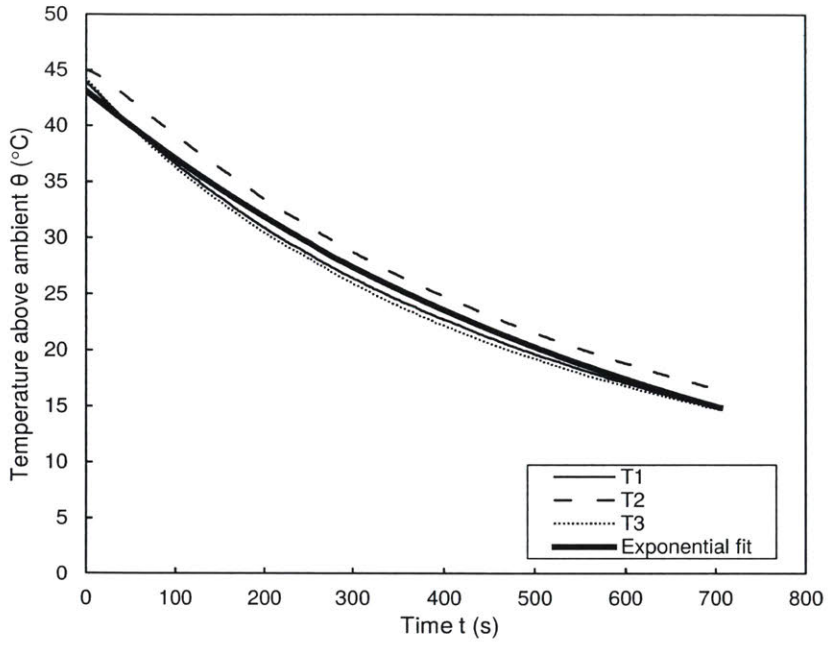

Figure 3-10: Full stack cool down with exponential fit $\theta = 43.1\exp(-t/664)$ where θ is °C above ambient and t is in seconds. T1, T2, and T3, represent thermocouple measurements in different parts of the stack.

battery stack, a temperature cut off of 60 °C lowers the achievable flight time to 90 s. Again, for a lower delivered power point such as 300 W, the battery stack can sustain a single discharge for several minutes and is not temperature-limited.

Cool down behavior of the stacked packs is again approximately an exponential decay of temperature, as seen in Figure 3-10. The stacked configuration shows a time constant of ~11 minutes rather than ~5 minutes as seen in the single pack, unstacked cool down behavior.

Considerations for selecting number of battery packs

Since the battery design is modular in nature and can satisfy a range of design points for the overall aircraft, a map of achievable flight times for a varying number of battery packs used and range of discharge power required is given in Figure 3-11. The primary considerations when selecting number of battery packs are more packs represents a higher input voltage to the power converter, higher discharge time, lower temperature for a given required power, and more weight. The red dot shows the

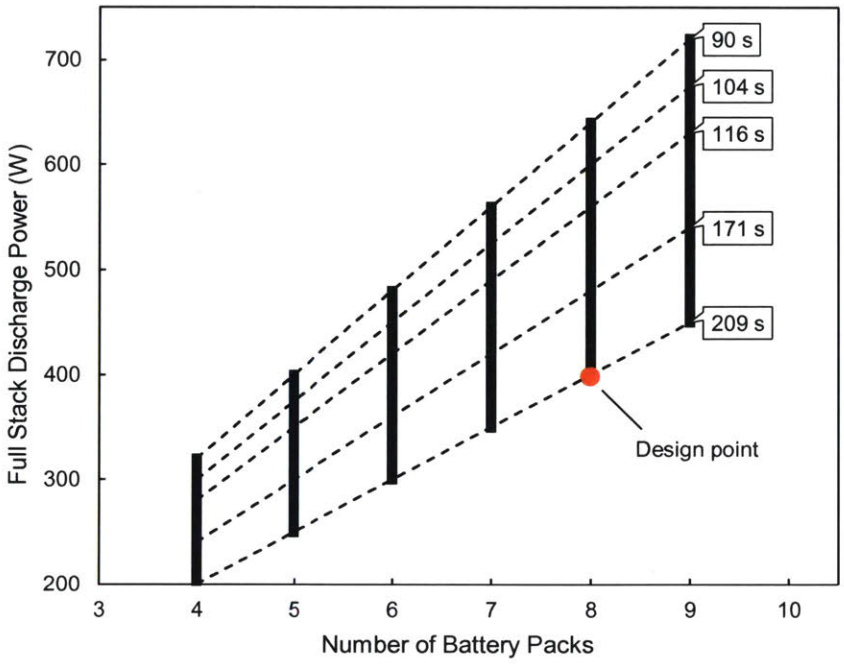

Figure 3-11: Achievable flight time as a function of number of battery packs used and power delivered. The vertical black bars represent possible discharge regions, the dashed lines represent the time that a discharge can be sustained, and the red dot represents the selected design point where flight tests were performed.

design point selected for the flight tests performed for and described in this thesis. Testing with the power converter shows a minimum input voltage of 160 V which translates into eight battery packs. The design point of the aircraft thrusters for flight testing is ~350 W which translates to ~400 W delivered from the battery stack.

3.1.3 Electrical system integration testing

After testing each subsystem separately to their design requirements, each of the subsystems are now connected and tested together. Possible failure modes for the airframe-power converter interface include damage to the power converter under a full-power arc, control logic behavior with a non-resistive and non-linear airframe load, and broadband noise interference from the thrusters affecting the logic board of the power converter. Possible failure modes for the power converter-battery interface include control logic on the power converter responding to the voltage transients of the battery, adverse heat transfer between the two subsystems, and unintended

discharging from the high voltage components to the nearby battery stack. Successful testing results of the battery-power converter are presented first and integrating both systems with the airframe thrusters follows.

Power converter resistive load testing

In preparation for integrating the batteries with the high voltage power converter, a series of tests were undertaken and passed where a power supply was programmed with various voltage ramps whose rate of change corresponded with observed voltage gradients of the battery stack during discharge (not shown).

Figure 3-12 shows full-scale resistive load testing of the high voltage power supply integrated with the battery stack. Input current is shown on the left and output voltage is shown on the right. When regulating only a resistive load on the output, the power converter accepts the slightly changing voltage of the battery stack without issue, and no issues such as discharging are noticed. The battery stack is physically separated from all high voltage components by approximately twice the thruster electrode gap spacing, and only experiences up to half of the potential difference that a thruster electrode pair sees, since the battery ground is connected to the middle of the 40 kV potential (i.e. a total of -20 kV and +20 kV relative to the battery stack). As such, no unintended discharging is seen.

The figure shows two other attributes of the output. The power supply output successfully creates a ~10 s ramp from 12.5 kV to 40 kV, which is implemented in order to minimize the chance of streamer formation of the thrusters, as noted earlier. There is also noise on the output voltage on the order of 1 kV. Testing with the thrusters is then done in order to determine whether this noise causes any negative effects such as arcing.

Full system testing with thrusters

After confirming performance with the power converter and batteries, the power converter was then used to power the airframe thrusters. First with a bench top power supply powering the input of the power converter, then with the battery stack

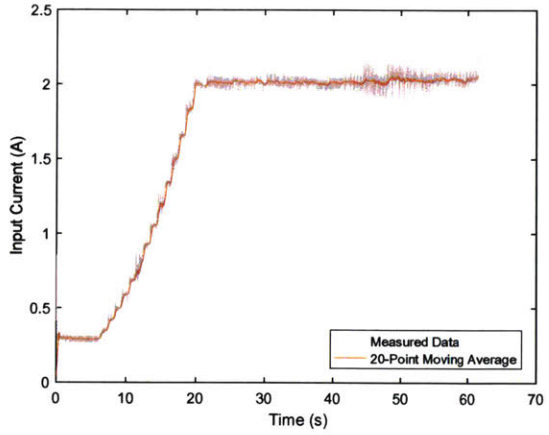

(a) Input current to power converter during resistive load test.

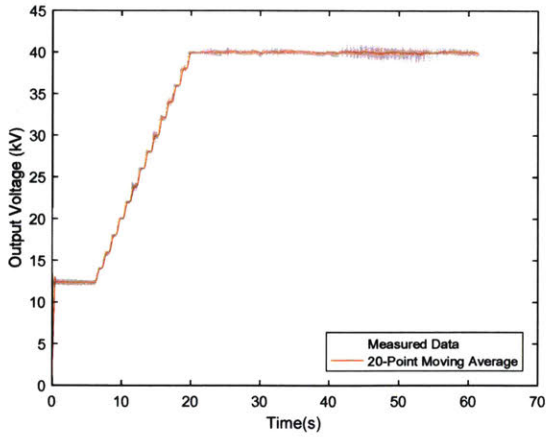

(b) Output voltage from power converter during resistive load test.

Figure 3-12: Resistive load power converter test results. Under 180 V input voltage, the power converter draws 2.02 A and outputs 40 kV to a resistance of 5.34 MΩ, resulting in a conversion efficiency of 82.3%.

powering the input of the power converter.

Figure 3-13 shows thrust measurements of the airframe thrusters. It shows a full trace of the thrusters alone, being powered by a bench top power supply, as well as thrust results with the high voltage power converter, and finally one set of thrust measurements with the electrical system fully integrated (battery stack, high voltage power converter, and thrusters). Tests were performed to confirm functionality with the power system packaged into the nosecone and mounted to the airframe, but thrust measurements were only taken when the nosecone was not mounted to the airframe due to weight constraints.

Thruster testing with the bench top power supply showed that the thrusters were not able to surpass approximately 38 kV without significant arcing. When the HVPC was connected to the thrusters, for unexplained reasons the HVPC could not reach higher voltages than 36.2 kV reliably. It is possible that slight damage, continued use, or bending of the diode heat sinks which might induce small corona discharge flows between them could be partial causes.

The integrated power system results show approximately 50 mN more thrust than the thruster only data. The maximum voltage and thrust of the fully integrated

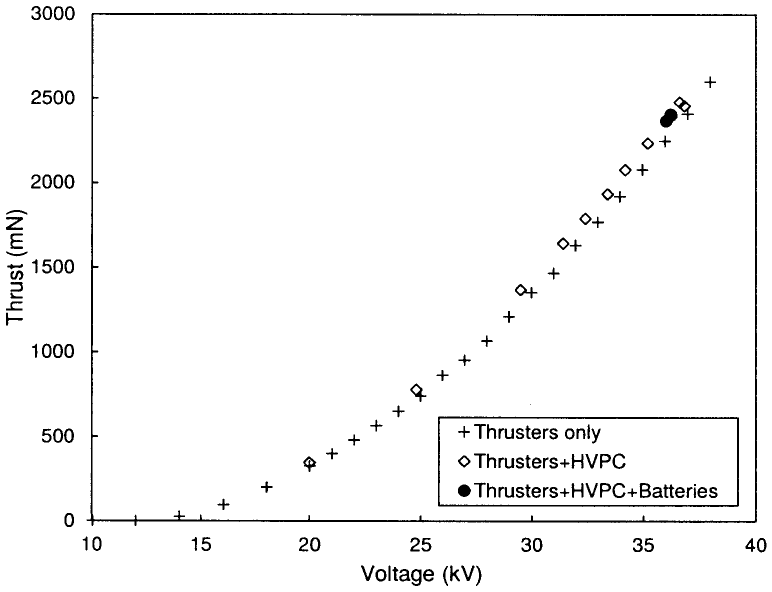

Figure 3-13: Thrust vs voltage for the airframe thruster array. Results are shown for the different stages of integrated testing with the thrusters. The highest thrust value for the thrusters + HVPC + battery stack was used during flight tests.

system is 36.2 kV and 2.44 N, respectively, and is used as the set point for the flight tests.

Figure 3-14 shows other measures of the airframe thrusters, and Table 3.1 gives the setpoint of the propulsion system for the flight tests.

Table 3.1: Voltage, thrust, and power of airframe thrusters used for flight testing.

Attribute	Value
Voltage	36.2 kV
Thrust	2.44 N
Power	340 W
T/P	7.2 N/kW

3.2 Communication system

E-field and noise

Testing of the communication system is performed to ensure the system worked while in the presence of the electric fields and electromagnetic noise that the thrusters may

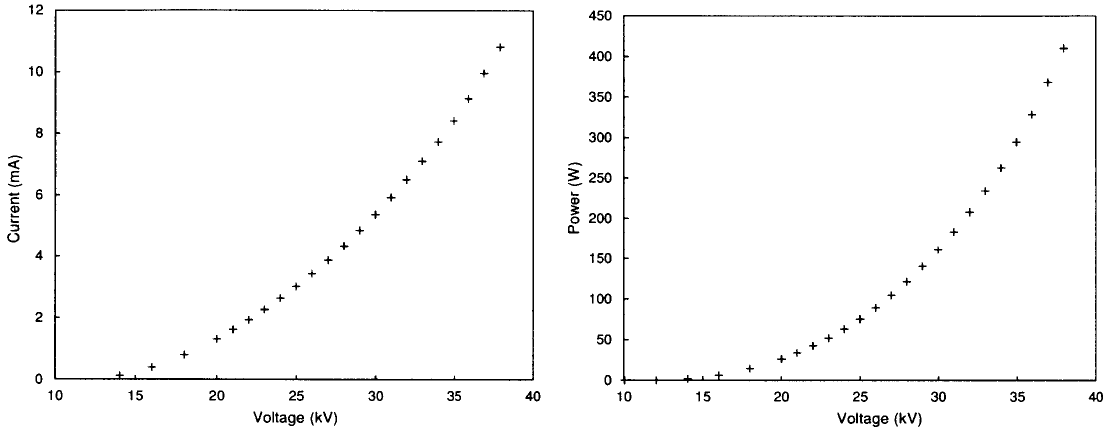

(a) Current vs Voltage

(b) Power vs Voltage

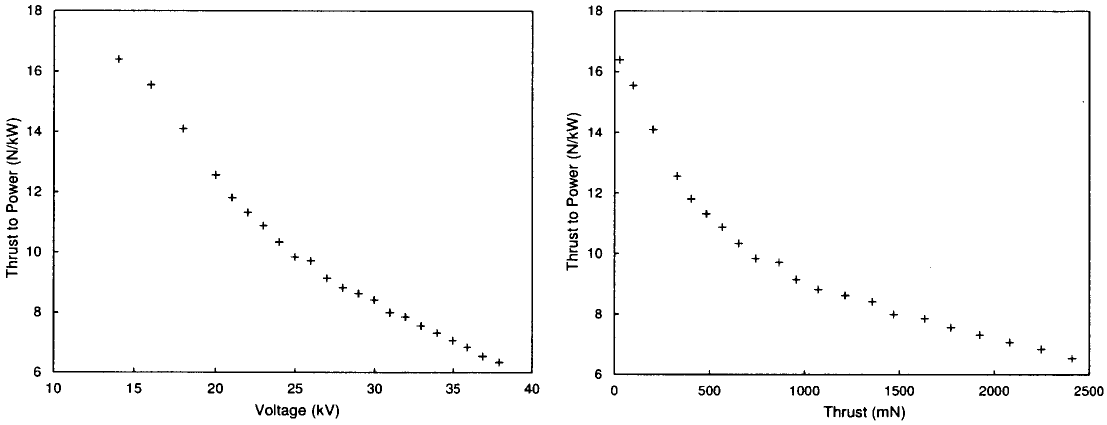

(c) Thrust to Power vs Voltage

(d) Thrust to Power vs Thrust

Figure 3-14: Thrust and power draw behavior of the airframe thruster array.

generate when on. Recall that there are two RC receivers on the aircraft: one on the tail to control the tail servos, and one in the nosecone to provide the throttle signal to the power converter.

An RC receiver is placed approximately where it would be positioned in the nosecone and a servo is connected and given movement commands from the receiver while the thrusters are turned on. The receiver on the tail is also given commands periodically and the test passes, confirming the communication system design is not adversely affected by the thrusters.

Range

The user in control of the RC remote took it approximately 200 m away from the testing area and outside. The above test was conducted again and passed, confirming that range was not diminished below the needs of the flight testing, which would be performed in a testing area of dimensions less than 100 m.

3.3 Aircraft structure

After redesigning the main wing and the tail of the aircraft. A propeller is secured to the airframe so it can be flown to assess the control authority of the new tail and the stability of aircraft.

3.3.1 Propeller testing

An electric propeller system is attached to the aircraft and flown. The aircraft is designed to fly in a straight line, so adquate control authority is defined here as the amount of pitch and yaw control required to correct for any disturbances during flight. Flying the aircraft with the redesigned tail showed that the tail provided adequate control authority.

3.4 Launcher

In order to confirm that the launcher system had structural integrity, tests were conducted where a 2 kg weight was launched 10 times and the system was inspected for any signs of damage. Points of interest were the structural integrity of the legs, deceleration system, and the front carriage. Approximate launch speed measurements were also made from footage taken of the launches, and used to calibrate the energy based model presented in Section 2.4.1.

Additionally, the aircraft was placed on launcher and powered to 40 kV and held for 1 minute. No arcing occurred, confirming that the launcher allows the aircraft to be powered on before launch.

Chapter 4

Flight testing

Flight tests were performed in the MIT duPont Gymnasium. Both unpowered and powered flight tests were conducted. Due to its size, the duPont Gym allowed flight tests on the order of 5 s but the vehicle is capable of flying for multiple minutes on a charge.

4.1 Experimental setup

A top-down view of the experimental setup for the flight tests is schematically shown in Figure 4-1. A side view of the coordinates, velocities, and forces in the xy flight plane, as well as the aircraft body coordinate frame are defined in Figure 4-2. The coordinate frames are defined below and after this, the rest of this section describes in detail the data collection technique and rationale, the equipment used, and the calibration process required to translate images from the camera into useful measurements.

Coordinate frames

Two coordinate frames are used. The world frame's origin is on the ground at the end of the launcher, and is positioned such that the flight path lies in the xy plane. The x direction points forward, the y direction points up (opposite the gravity vector), and z is completed by forming a right-handed coordinate system. It is an inertial

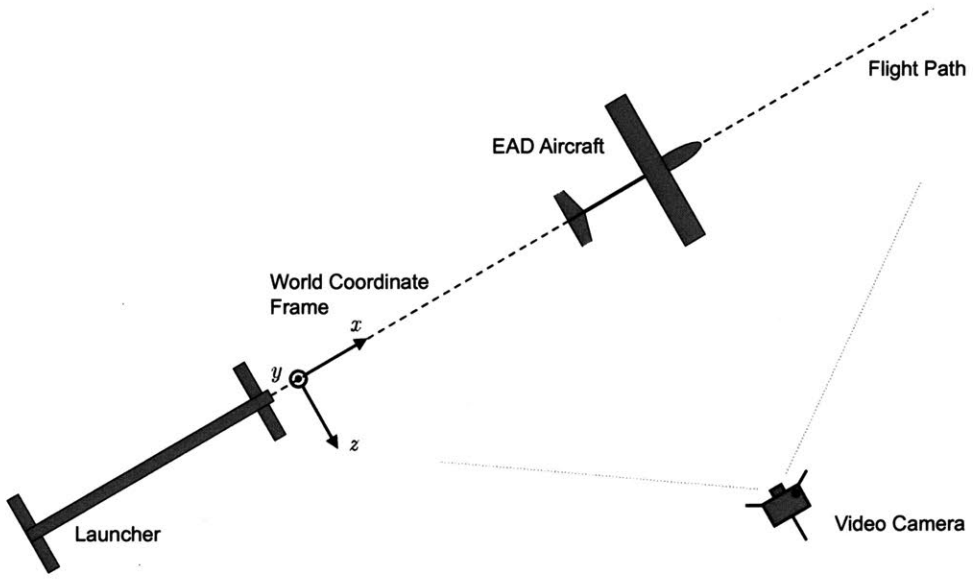

Figure 4-1: Top View: Experimental flight setup and world coordinate frame. The aircraft is launched and flown along a straight path while a video camera records its motion. The footage is then translated into world x and y velocities before further analysis.

coordinate frame.

The other coordinate frame is the body frame, which is shown in Figure 4-2. Its origin coincides with the world frame, but rotates about the z direction so that the body direction x' always points in the direction of the flight velocity. Therefore, lift force always acts along the body y' direction, drag acts along $-x'$, and thrust acts along x'. The angle between the x axis and the x' axis is labeled the aircraft elevation angle θ.

4.1.1 Overview of the data collection system

Vehicle velocity as a function of time is used in order to estimate lift, drag, and thrust characteristics of the aircraft. As shown in Figure 4-1, the aircraft motion is recorded by a camera that is approximately 15 m away in the z direction, and aimed perpendicular to the flight path. A laser pointing system is used when setting up the camera and flight path to ensure the camera is pointed perpendicular to the flight

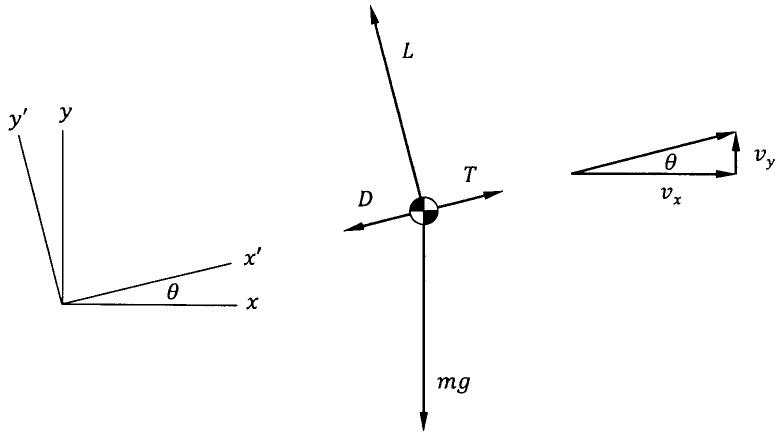

Figure 4-2: Side View: Forces, velocities, and coordinate frames. The the world xy plane as shown in Figure 4-1 and the $x'y'$ body coordinate plane, rotated by the aircraft elevation angle θ.

path. Pointing accuracy of within 1° is achieved.

The camera used is a GoPro Hero 5 Black. Factors considered include the capability to record in high resolution (2704 × 1520 at 30 frames per second) and that it uses a fixed aperture, meaning that a calibration single process will be accurate for all images captured.

Converting pixels to world coordinates

The process of converting pixel measurements from the images the camera generates into measurements of the photographed scene expressed in meters is adopted from Collins [17] and is described here. The camera is first calibrated, which is a process that determines the camera intrinsics and lense distortion coefficients. The calibration process is described in Section 4.1.2. Once the camera is calibrated, the relationship between a pixel coordinate and a world coordinate can be used, which is defined as

$$\begin{bmatrix} x_p & y_p & 1 \end{bmatrix} = \begin{bmatrix} x & y & z & 1 \end{bmatrix} \begin{bmatrix} R \\ t \end{bmatrix} \begin{bmatrix} K \end{bmatrix}, \tag{4.1}$$

where (x_p, y_p) is the location of the image pixel of interest (pixels) measured from the top left corner of the image, x, y, z is the corresponding location of the point expressed

in the world frame (m), R is the rotation matrix between the camera-centric frame and the world frame, t is the translation vector between the camera-centric frame and the world frame (m), and K is the camera's intrinsics matrix, which is

$$K = \begin{bmatrix} f_x & 0 & 0 \\ s' & f_y & 0 \\ c_x & c_y & 0 \end{bmatrix}, \tag{4.2}$$

where f_x, f_y are the camera focal lengths in the camera in the x_p and y_p directions expressed in number of pixels of the image sensor (pixels), s' is the skew parameter, and c_x, c_y is the optical center of the image (pixels). The skew parameter is a measure of misalignment between the camera image sensor and the lens and is assumed zero.

4.1.2 Camera calibration and optimization

The camera lens introduces distortion which makes straight lines appear curved. If the lens distortion coefficients are known, they can be used to undistort the images, where then the relationships presented above can be used to convert pixel coordinates into world unit coordinates in the desired coordinate frame.

Governing equations

Image undistortion is accomplished through MATLAB's Image Processing and Computer Vision toolbox. This toolbox also offers a camera calibration estimator based on a model that uses the pinhole camera [18] and lens distortion [19], but the output from this tool was found to produce measurements that had inaccuracies of >10%. To solve this, the same pinhole and radial distortion model (2-parameter) is adopted, where the relationship between distorted pixel location $(\bar{x}_{\text{p,distorted}}, \bar{y}_{\text{p,distorted}})$ of an unaltered image and the undistorted pixel location $(\bar{x_p}, \bar{y_p})$ is

$$\bar{x}_{\text{distorted}} = \bar{x} + (2k_1\bar{x}\bar{y} + k_2(r^2 + 2\bar{x}^2)), \tag{4.3}$$

$$\bar{y}_{\text{distorted}} = \bar{y} + (k_1(r^2 + 2\bar{y}^2) + 2k_2\bar{x}\bar{y}), \tag{4.4}$$

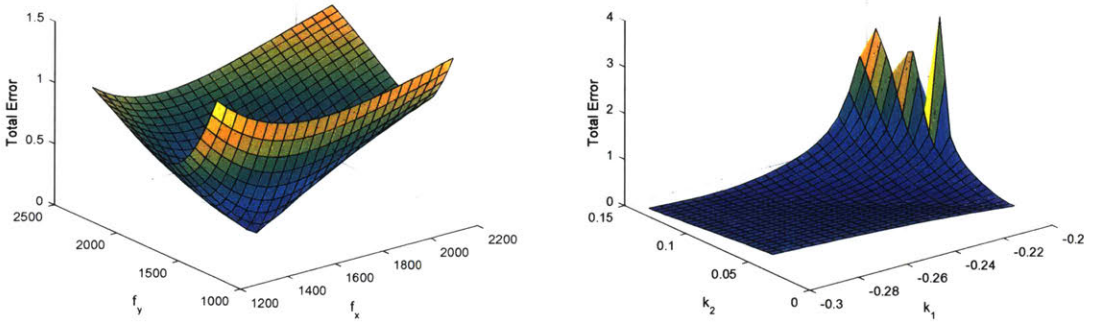

(a) Varying focal lengths, holding the radial lens coefficients constant.

(b) Varying radial lens coefficients, holding the focal lengths constant.

Figure 4-3: Measurement error resulting from varying the four considered parameters. Minimum error is found at $f_x = f_y = 1553$, $k_1 = -0.230$, and $k_2 = 0.0498$.

where $r^2 = \bar{x}^2 + \bar{y}^2$ and overbars denote normalized image coordinates, defined as

$$\bar{x} = \frac{x_p - c_x}{f_x}, \tag{4.5}$$

$$\bar{y} = \frac{y_p - c_y}{f_y}. \tag{4.6}$$

The four tuning parameters in the above equation relationships are f_x, f_y, k_1, and k_2. The next section describes the process used to determine of these four parameters such that accurate measurements could be made.

Calibration scene and optimized measurement results

The flight testing area was set up as though flight tests were to be performed, but poles of known length were set up at known intervals along the flight path, and images were taken. The pixel locations of known points were recorded and then used to calculated the distances between them. The error between those measurements and the true values were compounded and used as the objective function in an optimization search over the four variables f_x, f_y, k_1, and k_2. The error minimization and optimized values are shown in Figure 4-3.

The Images of the calibration scene before and after the undistortion process are

(a) Original (b) Undistorted

Figure 4-4: Images of the flight test and calibration scene shown on the left in its original form and on the right in its undistorted form.

shown in Figure 4-4. The optimized parameters result in an rms measurement error below 1% of the true values.

4.2 Data Analysis

A Kalman filter is used to filter the velocity measurements from the video footage. The filtered velocities are used to calculate the forces acting on the aircraft, and the aircraft's total energy throughout the flight tests. The Kalman filter is described first, a discussion of thrust variation with forward speed follows, and the equations of motion that govern the flight tests are given before the results are presented.

4.2.1 Kalman filter design

Kalman filtering is commonly used in aerospace applications as a way to make an estimate based on multiple input measurements, which may include a physical model. For example, Grillo et al. [20] employ a Kalman filter on several UAVs to estimate flight parameters.

A discrete time Kalman filter is implemented to combine the velocity data derived from the video footage with a motion model of the system. Adopting common notation, the states x of the system are the velocities v_x and v_y expressed in the world

frame, and

$$x_{k+1} = Ax_k + Bu_k, \tag{4.7}$$

$$\begin{bmatrix} v_x \\ v_y \end{bmatrix}_{k+1} = \begin{bmatrix} 1 & 0 \\ 0 & 1 \end{bmatrix} \begin{bmatrix} v_x \\ v_y \end{bmatrix}_k + \begin{bmatrix} \frac{\Delta t}{m} & 0 \\ 0 & \frac{\Delta t}{m} \end{bmatrix} \begin{bmatrix} -D\cos\theta - L\sin\theta \\ L\cos\theta - D\sin\theta - mg \end{bmatrix}_k, \tag{4.8}$$

where k denotes the current time step.

Covariance matrices

The filter incorporates measurement noise and process noise, which relate to uncertainty in the video measurements and in the motion model, respectively. The two uncertainties are assumed independent so the process-measurement covariance matrix is the identity matrix, I.

The measurement noise w_m is

$$w_m = \begin{bmatrix} \sigma_{v_x} \\ \sigma_{v_y} \end{bmatrix}_m, \tag{4.9}$$

where σ denotes standard deviation. The measurement covariance matrix Q_m is

$$Q_m = E(w_m {w_m}^T), \tag{4.10}$$

where E denotes expected value. The measurement noise is derived from the video data, as shown in Figure 4-5. In order to estimate the noise of the measurement data, a smoothing spline (shown as the black line) is fit with smoothing parameter $P = 0.998$ and used as a basis to calculate the standard deviation against.

The process noise w_p is

$$w_p = \begin{bmatrix} \delta_{v_x} \\ \delta_{v_y} \end{bmatrix}_p, \tag{4.11}$$

where δ denotes an uncertainty derived from the motion model. The process covariance matrix Q_p is

$$Q_p = E(w_p {w_p}^T), \tag{4.12}$$

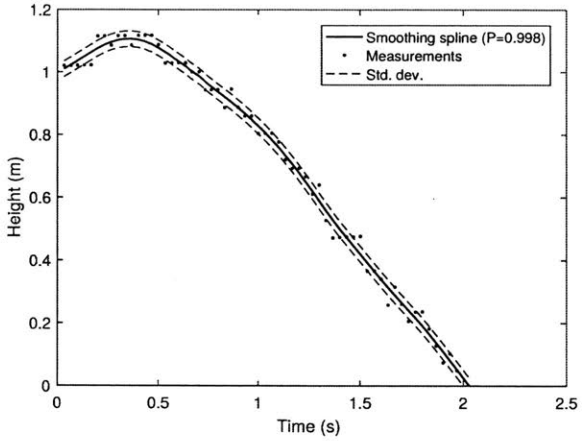

Figure 4-5: Vertical (y) data from one video measurement run. Typical behavior of measurement noise is seen which is used for a covariance matrix in the Kalman filter.

where E again denotes expected value.

In order to estimate the uncertainty in the motion model, we examine the difference in velocity that it predicts over the course of one time step. Only the x-direction is shown here for brevity. The velocity change Δv_x over one time step Δt is

$$\Delta v_x = \frac{\Delta t}{m}(-D\cos\theta - L\sin\theta). \tag{4.13}$$

Assuming that only the drag D, lift L, and elevation angle θ are uncertain, and that the remaining variables mass m and time step Δt are known precisely, a standard uncertainty propagation can be used. The uncertainty in the velocity change $\delta\Delta v_x$ over one time step is

$$\delta\Delta v_x = \sqrt{\left(\frac{\partial\Delta v_x}{\partial D}\delta D\right)^2 + \left(\frac{\partial\Delta v_x}{\partial L}\delta L\right)^2 + \left(\frac{\partial\Delta v_x}{\partial\theta}\delta\theta\right)^2}. \tag{4.14}$$

The nominal values used for L and D are taken as the values predicted by the GPkit model, and the respective uncertainties δL and δD are 2 N and 0.2 N respectively, meaning that we assign an uncertainty of approximately 10% to the lift and drag values predicted by the GPkit model. Note that $\delta\theta$ is an implicit function of Δv_x and Δv_y, but iterating on the uncertainty equation shows that this term is small

compared to the others and as such is neglected.

Filter performance

The behavior of the Kalman filter is shown in Figure 4-6 where filtered and unfiltered velocity data from one powered flight is shown. On the left is x velocity and on the right is y velocity.

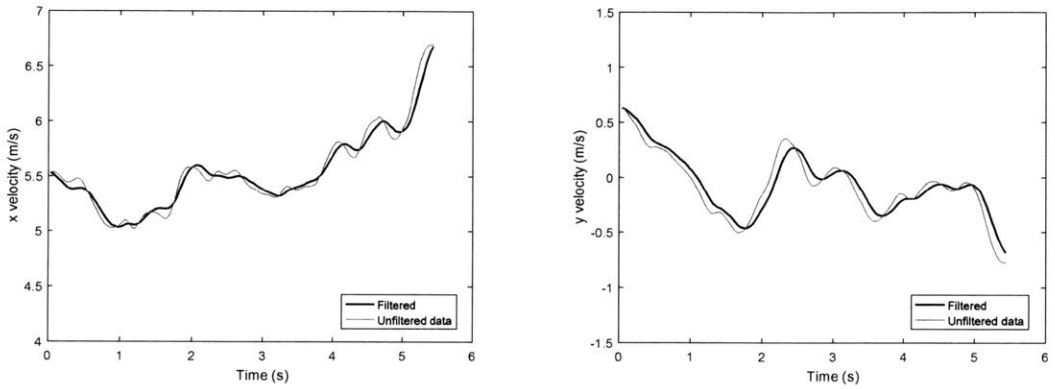

(a) v_x data (b) v_y data

Figure 4-6: Representative output from Kalman filter. Data is from powered flight 2 and x velocity is shown on the left while y velocity is shown on the right. The light grey line is the unfiltered data and the black line is the output from the filter.

4.2.2 Net thrust and forward speed

When forward speed of the system is introduced, a precise definition of thrust is necessary. The forces considered here are shown in Figure 4-7.

In estimating the wind speed of the neutral fluid u_{iw} generated by the asymmetric corona discharge, Roth et al. [21] proposed that electrostatic pressure trades exactly for dynamic pressure, or

$$\frac{1}{2}\epsilon E^2 = \frac{1}{2}\rho_f u_{\text{iw}}^2 \Rightarrow u_{\text{iw}} = \sqrt{\frac{E^2\epsilon}{\rho_f}} \approx \sqrt{\frac{V^2\epsilon}{L^2\rho_f}}, \tag{4.15}$$

where ϵ is permittivity, $E \approx \frac{V}{L}$ is electric field strength, V is voltage, L is the electrode gap distance, and ρ_f is neutral fluid density. This dependence was empirically

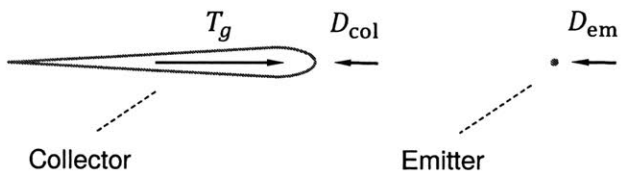

Figure 4-7: Forces acting on an emitter, collector pair. Gross thrust T_g, collector drag D_{col}, and emitter drag D_{em}.

confirmed by Moreau et al. [22].

This is relevant to the drag that the the emitters and collectors produce, even when in a static test environment. That is, the thrust measured on the static thrust rig equals gross thrust minus drag due to the induced ionic wind. Static thrust is given by

$$T_{\text{static}} = T_g - D_{\text{col}} - D_{\text{em}} \tag{4.16}$$

$$= T_g(V) - C_{D,\text{col}} A_{\text{col}} q_{\text{col}} - C_{D,\text{em}} A_{\text{em}} q_{\text{em}} \tag{4.17}$$

$$= T_g(V) - (C_{D,\text{col}} A_{\text{col}} + C_{D,\text{em}} A_{\text{em}}) \left(\frac{1}{2}\epsilon E^2\right), \tag{4.18}$$

where q denotes dynamic pressure and T_g is shown here as a function of operating voltage V. The last line assumes that the collector and emitter both see the induced dynamic pressure due to the electrostatic pressure. Note that T_{static} here is distinct from T in other literature, where the former incorporates the inherent drag of thruster geometry and the latter usually refers to gross thrust, labeled T_g in this analysis.

When there is a nonzero flight speed, consider the force balance again. The net

force on the emitter-collector pair, F_{net}, is

$$F_{\text{net}} = T_g(V) - C_{D,\text{col}} A_{\text{col}} q_{\text{col}} - C_{D,\text{em}} q_{\text{em}} A_{\text{em}} \tag{4.19}$$

$$= T_g(V) - (C_{D,\text{col}} A_{\text{col}} + C_{D,\text{em}} A_{\text{em}}) \left(\frac{1}{2}\rho v^2 + \frac{1}{2}\epsilon E^2\right) \tag{4.20}$$

$$\begin{aligned} = T_g(V) &- (C_{D,\text{col}} A_{\text{col}} + C_{D,\text{em}} A_{\text{em}}) \left(\frac{1}{2}\epsilon E^2\right) \\ &- (C_{D,\text{col}} A_{\text{col}} + C_{D,\text{em}} A_{\text{em}}) \left(\frac{1}{2}\rho v^2\right) \end{aligned} \tag{4.21}$$

$$= T_{\text{static}} - (C_{D,\text{col}} A_{\text{col}} + C_{D,\text{em}} A_{\text{em}}) \left(\frac{1}{2}\rho v^2\right). \tag{4.22}$$

The result is that thrust with nonzero flight speed is the thrust that is measured in a static thrust test, minus a drag force equal to the amount of drag the thrusters would generate when they are off. This allows the use of static thrust test data in the calculation of drag for the powered flight tests. An assumption made here, however, is that gross thrust does not change with forward speed. This is not strictly true, but Masuyama and Barrett [8] estimate the effects of bulk neutral fluid velocity on gross thrust to power, $\frac{T_g}{P}$, and find that

$$\frac{T_g}{P} = \frac{\rho E L A}{V_a \rho (\mu E + v) A} = \frac{1}{\mu E + v}. \tag{4.23}$$

The ion drift velocity μE of this system is >100 m/s and the flight speed is approximately 5 m/s, so variation in gross thrust with forward speed is neglected and seen to be much smaller than the drag on the system due to nonzero forward speed.

For the remainder of this document, T and D refer to the thrust and drag as defined above. That is $T = T_{\text{static}}$ and D = remaining force in the body x' direction.

4.2.3 Equations of motion

Aircraft motion is typically expressed as six kinematic relations that relate the aircraft velocity and orientation rate in the body frame to the world frame, and six equations of motion that relate linear momentum and angular momentum in the body frame to the world frame. Since the measurement system employed measures velocities in

the inertial earth frame, we use this data directly to calculate forces throughout a flight. Only longitudinal motion (pitch, "forward", and "up") is considered. The x and y linear momentum equations are used to calculate the forces on the aircraft, which are then rotated into the body frame in order to decompose them into lift, drag, and thrust. This relationship is

$$\begin{bmatrix} T-D \\ L \end{bmatrix} = \left[R(\theta)\right] \left(\frac{d}{dt} \begin{bmatrix} mv_x \\ mv_y \end{bmatrix} + \begin{bmatrix} 0 \\ mg \end{bmatrix} \right). \tag{4.24}$$

Excess thrust $T_{\text{excess}} = T - D$ can equivalently be calculated with the energy relationship

$$T_{\text{excess}} = \frac{1}{v} \left(\frac{m}{2} \frac{d}{dt} \left(v^2\right) + mg \frac{d}{dt} y \right) \tag{4.25}$$

where $\theta = \tan^{-1}(v_y/v_x)$. When unpowered flights are performed, L and D are solved for directly. When powered flights are performed, L and T_{excess} are solved for, but as derived in the Section 4.2.2 we assume that the thrust is the same as that measured on the static thrust stand which allows us to solve for drag by $D = T - T_{\text{excess}}$.

Specific excess power, SEP, is a measure of the rate at which the aircraft can increase its total energy, normalized by its weight. SEP is defined as

$$\text{SEP} = \frac{T_{\text{excess}} v}{mg} \tag{4.26}$$

and is also calculated for each powered flight.

Ground effect

Ground effect may decrease the drag of the aircraft. When a lifting element flies close to the ground, the vortices that it sheds interact with the ground to effectively lower induced drag. To estimate how much the flight tests may have been affected by ground effect, Raymer [16] gives

$$\frac{Q_{\text{eff}}}{Q} = \frac{33(h/b)^{3/2}}{1 + 33(h/b)^{3/2}}, \tag{4.27}$$

where Q is induced drag without ground effect, Q_{eff} is induced drag with ground effect, h is height above the ground, and b is wingspan. For an average flying height of the wingtips of about 1.5 m, this estimates the induced drag to be diminished by approximately 15%. The GPkit model predicts the induced drag of the aircraft to be approximately 0.45 N., so under these flight conditions, the total drag reduction due to ground effect is estimated to be 0.07 N, or approximately 3% of the total drag on the aircraft, predicted by the GPkit model.

4.3 Results

Seven unpowered and seven powered flights were performed. In all cases, the aircraft was launched and a remote pilot controlled the tail elevator and rudder in an effort to find and hold trim. Figure 4-8 shows the trajectories of all flights.

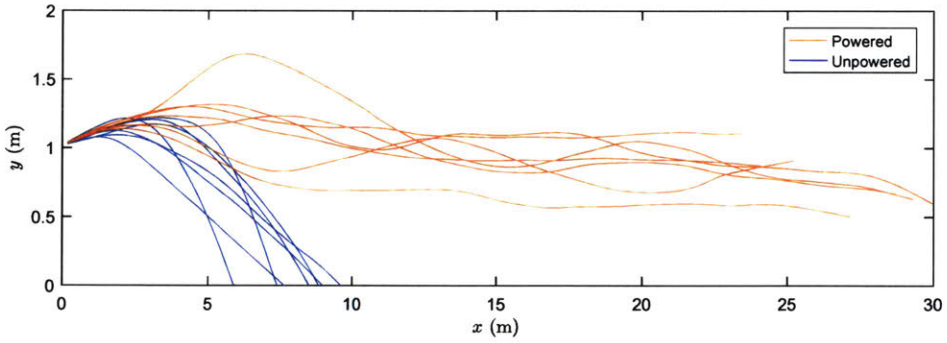

Figure 4-8: Trajectories of the unpowered and powered flights.

Throughout a trajectory, the aircraft velocity is not constant so to account for this, Figure 4-9 shows the total energy of each flight.

Figure 4-10 shows the specific excess power of each of the powered flights. The mean values of two flights are positive, but the standard deviation of all flights overlap zero.

Table 4.1 tabulates the average C_L/C_D, the total energy gained ΔE, and the average SEP for each of the powered flight tests. The mean and standard deviation over all flight tests for each measure is given at the bottom. Angle brackets denote

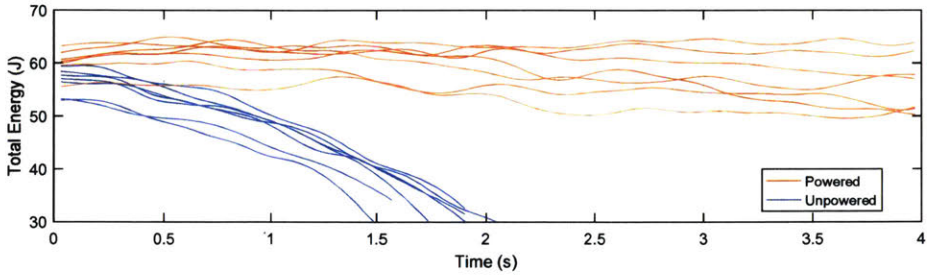

Figure 4-9: Total energy of all unpowered and powered flights.

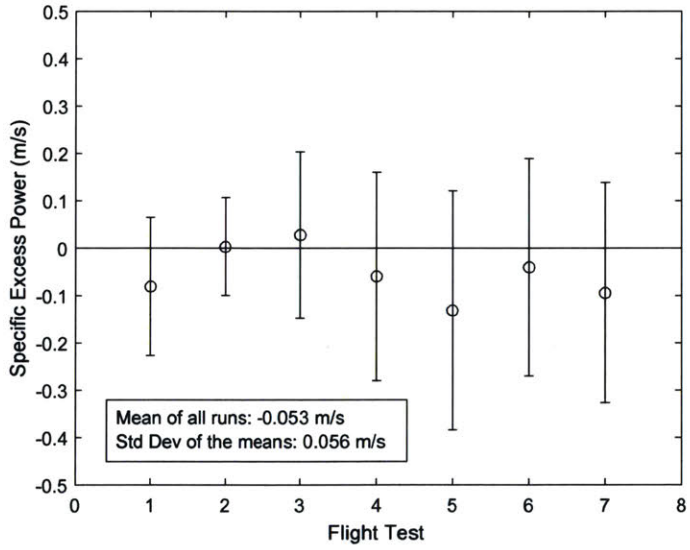

Figure 4-10: Specific excess power of each of the powered flight tests. A circle denotes the average for a flight test and the bar denotes the standard deviation throughout a flight.

Table 4.1: Average data from each powered flight test.

Flight test	$\langle \frac{C_L}{C_D} \rangle$	ΔE (J)	$\langle$SEP$\rangle$(m/s)
1	9.04	-6.26	-0.081
2	9.90	0.01	0.003
3	11.51	3.60	0.028
4	10.22	-4.35	-0.060
5	9.33	-9.70	-0.131
6	10.74	-2.86	-0.040
7	9.48	-7.87	-0.094
Mean	10.03	-3.92	-0.053
Std Dev	0.87	4.61	0.056

mean value. The average C_L/C_D is 10.0, which is less than the C_L/C_D predicted by the GPkit model, which is 10.3.

This analysis shows that the powered flight tests were close, but likely did not achieve steady-level flight. However, the flights were conducted at below the full design power, which suggests that steady level flight with this aircraft is likely to be possible when run at 40 kV rather than 36.2 kV.

Chapter 5

Conclusions

EAD propulsion is a means of electric thrust generation with no direct emissions (although ozone is generated), no moving parts, and is nearly silent. These advantages over more mature propulsion technologies have motivated the development of an aircraft to demonstrate steady level-flight of an EAD-propelled aircraft.

This thesis presented the design and testing of several subsystems of an EAD aircraft and its flight testing. The subsystems focused on were the power system, the communication system, the tail, and the launcher.

Lithium polymer battery cells were chosen as the energy source for the aircraft because this battery chemistry delivers higher power density than other chemistries commercially available. The battery stack is built and shown to exceed the the required maximum of 700 W for 60 s. Thermal behavior of the batteries was found to be the limiting factor of achievable discharge time only near its maximum power delivery, and is not a limiting factor for the design point of these tests, which was approximately 400 W. The launcher was designed to allow the high voltage aircraft to reach full power before being launched, and then to launch the aircraft reliably to at least its nominal flight speed of ~5 m/s. The tail produced a stable aircraft and allowed control of it throughout the flight tests.

A camera-based flight data collection system was also designed and implemented and a method was developed for converting the output from the camera into useful flight data. This system was used to calculate the lift and drag of the aircraft throug-

hout a flight, as well as the aircraft's total energy, and can be used in future flight testing.

Flights were judged to be steady-level if the total energy of the aircraft was held constant, or increased throughout a flight. Data suggests that two of the seven flights gained total energy, although the uncertainty associated with each flight overlaps zero.

However, reasons that this was the case are first that the EAD aircraft was flown with the power power system at 36.2 kV, which is below the maximum design voltage of 40 kV. This was due to both the power converter and the thrusters both failing to reach the full 40 kV reliably, suggesting that future testing of the same aircraft may successfully demonstrate steady-level flight. Secondly, the aircraft had features that created drag and were not included in the GPkit model, such as exposed wiring, a rough fuselage, and draggy side panels. These are both areas in which the aircraft may be modified to make flight with excess power more likely. If however, those prove not to allow steady-level flight, the power system has been tested to deliver up to approximately 75% more than the design point of these flight tests, so it is possible that a different iteration of the aircraft design can be found without major modifications to the power system.

Beyond these modifications, two technologies that might enable a more powerful and longer endurance EAD aircraft are power system density and thruster technology. The power system of this aircraft accounted for approximately 40% of its total mass, meaning increased power and energy density of battery technology, and decreased weight of power converter technology will have a large impact on reducing overall aircraft mass, and therefore increasing range and/or specific excess power. Secondly, a more efficient thruster technology where mechanism for the generation of ions is distinct from their acceleration (the corona discharge thruster employed in this aircraft uses one electric field for both processes) might enable higher thrust densities than possible with the current technology.

References

[1] E. A. Christensen and P. S. Moller. "Ion-neutral propulsion in atmospheric media". In: *AIAA Journal* 5.10 (1967), pp. 1768–1773.

[2] B. L. Owsenek and J. Seyed-Yagoobi. "Theoretical and experimental study of electrohydrodynamic heat transfer enhancement through wire-plate corona discharge". In: *Journal of Heat Transfer* 119 (1997), pp. 604–610.

[3] O. M. Stuetzer. "Ion drag pumps". In: *Journal of Applied Physics* 31.1 (1960), pp. 136–146.

[4] F. O. Thomas, M. Corke T. C .and Iqbal, A. Kozlov, and D. Schatzman. "Optimization of dielectric barrier discharge plasma actuators for active aerodynamic flow control". In: *AIAA Journal* 47.9 (2009), pp. 2169–2178.

[5] *Boeing current market outlook 2013-2032.* Technical report. The Boeing Company, Seattle, WA, 2013.

[6] S. H. L. Yim, G. L. Lee, I. H. Lee, F. Allroggen, A. Ashok, F. Caiazzo, S. D. Eastham, R. Malina, and S. R. H. Barrett. "Global, regional and local health impacts of civil aviation". In: *Environmental Research Letters* 10.3 (2015), p. 034001.

[7] A. Mahashabde, P. Wolfe, A. Ashok, C. Dorbian, Q. He, A. Fan, S. Lukachko, A. Mozdzanowska, C. Wollersheim, S. R. H. Barrett, M. Locke, and I. Waitz. "Assessing the environmental impacts of aircraft noise and emissions". In: *Progress in Aerospace Sciences* 47.1 (2011), pp. 15–52.

[8] K. Masuyama and S. R H. Barrett. "On the performance of electrohydrodynamic propulsion". In: *Proc. R. Soc. A.* Vol. 469. 2154. The Royal Society. 2013, p. 20120623.

[9] C. K. Gilmore and S. R. H. Barrett. "Electrohydrodynamic thrust density using positive corona-induced ionic winds for in-atmosphere propulsion". In: *Proc. R. Soc. A.* Vol. 471. 2175. The Royal Society. 2015, p. 20140912.

[10] C. K. Gilmore. "Electro-aerodynamic thrust for fixed-wing aircraft propulsion". PhD thesis. Massachusetts Institute of Technology, 2017.

[11] W. W. Hoburg and P. Abeel. "Geometric programming for aircraft design optimization". In: *AIAA Journal* 52.11 (2014), pp. 2414–2426.

[12] Y. He and D. J. Perreault. "Design and Implementation of a Lightweight High-Voltage Power Converter for Electro-aerodynamic Propulsion". In: *Workshop on Control and Modeling for Power Electronics.* IEEE, 2017.

[13] University of Illinois at Urbana-Chambagne Applied Aerodynamics Group. *Airfoil Coordinates Database.* 2017. URL: `http://m-selig.ae.illinois.edu/ads/coord_database.html`.

[14] M. Drela. "XFOIL: An analysis and design system for low Reynolds number airfoils". In: *Low Reynolds number aerodynamics.* Springer, 1989, pp. 1–12.

[15] M. Drela, S. Hall, P. Lagace, I. Lundqvist, G. Naeser, H. Perry, R. Radovitzky, I. Waitz, P. Young, and J. Craig. *16.01 Unified Engineering I, II, III, and IV.* Massachusetts Institute of Technology. 2005. URL: `http://ocw.mit.edu`.

[16] D. P. Raymer. *Aircraft Design: A Conceptual Approach.* 3rd. AIAA, 1999.

[17] R. Collins. *CSE486: Introduction to Computer Vision.* Pennsylvania State University. 2007. URL: `http://www.cse.psu.edu/~rtc12/CSE486/lecture13.pdf`.

[18] Z. Zhang. "A flexible new technique for camera calibration". In: *IEEE Transactions on pattern analysis and machine intelligence* 22.11 (2000), pp. 1330–1334.

[19] J. Heikkila and O. Silven. "A four-step camera calibration procedure with implicit image correction". In: *Proceedings on Computer Vision and Pattern Recognition, IEEE Computer Society Conference on.* IEEE. 1997, pp. 1106–1112.

[20] C. Grillo and F. Montano. "An Extended Kalman Filter-Based Technique for On-Line Identifcation of Unmanned Aerial System Parameters". In: *Journal of Aerospace Technology and Management* 7.3 (2015), pp. 323–333.

[21] J. R. Roth, D. M. Sherman, and S. P. Wilkinson. "Boundary layer flow control with a one atmosphere uniform glow discharge surface plasma". In: *Proceedings of the 36th AIAA Aerospace Sciences Meeting and Exhibit.* AIAA, 1998.

[22] E. Moreau and G. Touchard. "Enhancing the mechanical efficiency of electric wind in corona discharges". In: *Journal of Electrostatics* 66.1 (2007), pp. 39–44.